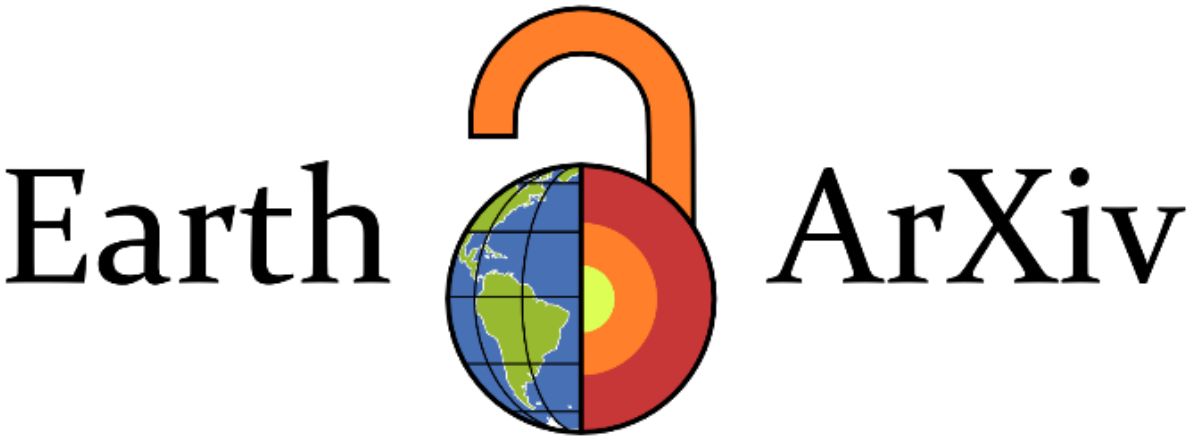

Influence of sea surface temperature patterns and mean warming on past and future Atlantic tropical cyclone activity

E. L. Levin[a] G. A. Vecchi,[b] W. Yang,[b]

[a] *Program in Atmospheric and Oceanic Sciences, Princeton University*

[b] *Department of Geosciences, Princeton University*

Corresponding author: Emma Levin, emma.levin@princeton.edu

ABSTRACT: This study investigates the relative contributions of large-scale thermodynamic and dynamic processes to decadal and multidecadal changes in Atlantic tropical cyclone (TC) activity, spanning the historical record since the late 19th century, and extending to 2100 projections. We employ a framework that decomposes TC counts into precursor disturbances that transition into fully developed storms, applied to multi-ensemble simulations of two TC-permitting atmospheric models. Using these models, we conduct controlled experiments with distinct SST forcings that isolate the influence of SST spatial patterns from that of global-mean warming on Atlantic TC activity. Our results show that decadal and multidecadal changes in TC frequency are primarily governed by two thermodynamic variables: potential intensity and moist entropy deficit. In the historical record, these variables reinforced one another, producing more robust trends in TC activity. In contrast, future projections suggest opposing influences, with one variable (potential intensity) becoming more favorable for TCs while the other (moist entropy deficit) becomes less favorable, leading to increased uncertainty in TC projections. We trace this shift to differences in relative warming between the tropical Atlantic and the broader tropics, underscoring that regional SST patterns, rather than the global mean warming rate, control both past variability and projected future changes in TC activity. Constraining future projected patterns of warming is therefore essential for improving the reliability of TC projections.

1. Introduction

Responsible for over $250 billion of inflation-adjusted losses in the U.S. between 2008 and 2017 (Klotzbach et al. (2018)), landfalling tropical cyclones (TCs) that form in the Atlantic Ocean are a major hazard for both coastal and inland communities in the U.S. and Caribbean. Further, it is crucial to understand the factors that have driven past fluctuations in Atlantic storm activity, and the extent to which anthropogenic warming might influence TCs in the future.

While several studies attempting to reconstruct a reliable historical record of Atlantic TCs generally disagree on the direction of the trend in Atlantic TC counts from the late-19th century to the present (Emanuel (2021a),Vecchi and Knutson (2008), Vecchi and Knutson (2011), Vecchi et al. (2021)), there is a growing understanding of a role for regional climate variability, warming patterns, and aerosol concentrations, rather than global mean anthropogenic warming, in driving past fluctuations in seasonal storm frequency. For instance, several studies indicate that natural climate modes, such as the Atlantic Multi-decadal Oscillation (Goldenberg et al. (2001); Klotzbach (2011b); Zhang and Delworth (2006)) and the El Niño Southern Oscillation (Klotzbach (2011a); Klotzbach et al. (2022); Patricola et al. (2016); Pielke and Landsea (1999); Xie et al. (2005)), along with their corresponding oscillating sea surface temperature patterns, can influence North Atlantic TC activity. Additionally, another explanation links past multidecadal fluctuations in Atlantic TC activity to the rise and subsequent decline of sulfate aerosol emissions, driven by global environmental regulations (Booth et al. 2012; Dunstone et al. 2013; Mann and Emanuel 2006; Murakami and Wang 2022).

Although there is a growing consensus that global warming contributes to an increase in peak TC windspeed and rainfall intensity (see reviews Knutson et al. (2020) and Walsh et al. (2019) and references therein), it remains unclear how seasonal TC counts will change in a warmer world (Knutson et al. (2020) and Sobel et al. (2021)). Most studies based on climate model simulations project a decrease or minimal change in global TC count (see reviews Knutson et al. (2020) and Walsh et al. (2019) and references therein), but there is much spread in projections for individual basins (Kossin et al. 2020). However, some dynamical modeling studies (e.g., Bhatia et al. (2018), Vecchi et al. (2019)) and statistical-dynamical downscaling efforts (e.g., Emanuel (2013), Emanuel (2021b)) predict an increase in global TC frequency due to anthropogenic global warming.

Several factors may explain the discrepancies in TC frequency projections across studies. First, these studies use various climate models with differing parametrization schemes and horizontal resolutions, ranging from tens to hundreds of kilometers, that may or may not resolve TCs and mesoscale processes (Camargo et al. (2020); Hsieh et al. (2023); Manganello et al. (2012)). Inconsistencies in TC projections may also stem from uncertainties regarding the impact of thermodynamic variables, particularly humidity, on TC genesis. For instance, saturation deficit represents the difference between the specific humidity of the atmosphere and its specific humidity at saturation (Olszewski (1986)). In a warmer world, the saturation deficit in the lower and mid-troposphere increases (Held and Soden (2000); Emanuel (2010, 2021a)). A higher saturation deficit would require an increased surface moisture flux to bring the atmospheric column to saturation, which could inhibit deep convection and cyclogenesis (Sobel et al. (2021), Tang and Camargo (2014)). This theory suggests that with a higher saturation deficit in a warmer world, TC activity would decrease (Camargo et al. (2014); Emanuel (2021a); Emanuel (2010); Lee et al. (2020); Lee et al. (2023); Vecchi et al. (2019)). However, several high-resolution models project an increase in TC activity (Bhatia et al. (2018); Vecchi et al. (2019)), despite a rise in saturation deficit. These studies suggest that the interplay between local thermodynamic and dynamic variables could play an important role in driving changes in TC activity. In the models that show a TC frequency increase, the reduced genesis favorability from changes in saturation is outweighed by an increase in pre-TC disturbances (known as 'seeds') (Vecchi et al. 2019; Hsieh et al. 2020).

Finally, inherent model biases and variations in projections of regional climate and sea surface temperature (SST) patterns, particularly in the Eastern Pacific and Atlantic basins (see review by Shaw et al. (2024) and references therein), could lead to differences in future TC projections. Atlantic TCs are sensitive to the relative average temperature of the tropical Atlantic compared to the rest of the tropics (Vecchi and Soden (2007); Villarini et al. (2011b)). Villarini et al. (2011b) show that the SST patterns explain much of the spread in projected North Atlantic TC frequency projections.

To investigate the relationships between large-scale environmental factors and TC activity, several indices have been developed (e.g., Bruyère et al. (2012); Emanuel and Nolan (2004); Emanuel (2010); Tippett et al. (2011); Wang and Murakami (2020)). These indices, known as genesis potential indices (GPIs), relate local environmental factors—such as potential intensity (PI), vertical

wind shear, and humidity—to TC activity. GPIs are typically calculated from monthly averages, representing regional climatology rather than instantaneous weather conditions (Sobel et al. (2021)). While GPIs have been used to predict the effects of future climate change on TC activity (e.g., Murakami and Wang (2022)), Camargo et al. (2014) found that most GPIs fail to capture future TC projections from atmosphere-only climate models. Moreover, these TC proxies show low skill in capturing interannual variability and multidecadal trends in TC activity compared to climate models that explicitly resolve TCs (Cavicchia et al. 2023), likely because they do not account for key physical processes involved in TC genesis, such as the formation of initial TC seeds.

As an alternative way to construct GPIs, Hsieh et al. (2020) present a framework for understanding how large-scale local environmental fields influence TC formation, explicitly accounting for the seed phase of formation. Unlike traditional GPIs (Emanuel (2022)), this approach divides tropical cyclogenesis into distinct phases, identifying the specific large-scale local factors relevant to each stage of TC development. This framework is motivated by a recognition that the feedbacks on development of TCs are different at different stages (Hsieh et al. 2020; Zhang et al. 2021), and thus the environmental controls on seeds and the likelihood of genesis to a mature TC may be different. This technique of separating TCs into seeds and a nondimensional probability that a seed transitions into a TC has proven useful for studying TCs across various timescales, including their annual cycle (Yang et al. (2021)) and over longer idealized climatic periods (Hsieh et al. (2022); Hsieh et al. (2023); Vecchi et al. (2019)). In this study, we extend the application of this framework to the long observed historical record, where it has not yet been applied. Additionally, we focus this approach on the Atlantic basin, where seed-like disturbances may be influenced by nonlocal factors, such as African Easterly Waves (Patricola et al. (2018), Ritchie and Holland (1999)).

Through this work, we aim to address the following research questions:

1. To what extent does the theoretical framework proposed by Hsieh et al. (2020) capture long-term observed and projected Atlantic TC variability?

2. To what extent do different environmental factors (both thermodynamic and dynamic) modulate Atlantic TCs in the observed and projected records, and how are these factors related to regional warming patterns versus globally-uniform warming?

To address these questions, we employ the seed-probability framework within a suite of state-of-the-art high-resolution atmosphere-only general circulation model experiments that have demon-

strated skill in simulating key characteristics of past TC activity (Chan et al. (2021), Chen and Lin (2011), Zhao et al. (2009), and Zhao and Held (2010)). We seek to identify the dominant large-scale environmental factors driving historical and future projected variations in Atlantic TC frequency. By utilizing atmosphere-only models forced by observed SSTs, we effectively isolate the influence SST patterns on TC activity.

2. Methods and data

a. Models and experiments

In this study, we employ two closely related global high-resolution atmospheric models from the Geophysical Fluid Dynamics Laboratory (GFDL): AM2.5-C360 and HIRAM (Zhao et al. (2009)), both of which have been used to study tropical cyclones (TCs). These models share the same dynamical core but differ in a number of their parameterizations (e.g. convection and cloud) and horizontal resolutions. AM2.5-C360 uses the relaxed Arakawa–Schubert convective parametrization scheme, while HIRAM uses the shallow parametrization method described in Bretherton et al. (2004) modified to allow for deep convection (Zhao et al. 2009). HIRAM, with a horizontal resolution of 50 km, has demonstrated skill in simulating various aspects of past TC variability (Chen and Lin (2011), Zhao et al. (2009), and Zhao and Held (2010)). AM2.5-C360, on the other hand, has a higher resolution of 25 km, and has been employed in prior studies to examine the influence of SSTs on tropical cyclone activity (Chan et al. 2021), the annual cycle of TCs (Yang et al. 2021), and the evolution of storm tracks under warming conditions (Kortum et al. 2024). The use of atmosphere-only models forced with prescribed SSTs provides a clean framework for isolating the role of SST patterns in shaping TC behavior.

We conducted two sets of experiments (Table 1) to isolate the effects of spatial patterns of SST change from global mean SST warming, one using the historical record and one using future projections. For the past historical period, in the first experiment, hereafter named *obs sst*, we generated ten ensemble members of AM2.5-C360 and five ensemble members of HIRAM. The models are forced by bias-corrected observed monthly sea surface temperatures (Chan et al. 2021) from the Hadley Centre Sea Ice and Sea Surface Temperature (HADISST) dataset for the period 1871–2019. Each ensemble member was initialized with different initial conditions but used the

same historical SST forcing. We decompose the SSTs in this experiment into several components:

$$SST_{\underline{obs\ sst}} = SST_{clim}(x, y, \text{mon}) + \langle SST' \rangle (t) + SST'(x, y, t), \tag{1}$$

where $SST_{clim}(x, y, \text{mon})$ represents the observed monthly climatology throughout the 1871-1890 period at each (longitude, latitude) point (x,y) for each month (January, February, ...), $\langle SST' \rangle (t)$ represents the observed spatially averaged mean anomaly for each month over the duration of the record (January 1871, February 1871, . . .) from the globally averaged 1871-1890 monthly climatology, and $SST'(x, y, t)$ represents the observed spatially varying anomaly at each point (x,y) for each month over the duration of the record (January 1871, February 1871, . . .) from the globally averaged 1871-1890 monthly climatology. Therefore, in the historical record that undergoes anthropogenic warming, $\langle SST' \rangle (t)$ represents the global mean warming while $SST'(x, y, t)$ represents the spatially varying pattern of SST change.

The second experiment, hereafter named *rm warming*, is the same as the first, except the radiative forcings are fixed at the year 1880 levels and the specified SSTs are modified in a way that the 15-year lowpass of global mean monthly SST anomaly (relative to the 1871-1890 monthly climatology) is subtracted at each ocean cell grid. Therefore, we remove the $\langle SST' \rangle (t)$ term in the *obs sst* record, so the SSTs for this experiment can be written in their decomposed form as:

$$SST_{\underline{rm\ warming}} = SST_{clim}(x, y) + SST'(x, y, t), \tag{2}$$

where the only difference from the *obs sst* SST forcing is the removal of the globally averaged warming signal $\langle SST' \rangle (t)$. Therefore, the differences between the *obs sst* and the *rm warming* experiments can be attributed to spatially averaged mean warming and the direct atmospheric effect of changing radiative forcing. Thus, if we find minimal differences in the TC activity and their environmental controls between these simulations, we can argue that mean warming played a minimal role in driving TC variability during the historical record. We run this experiment in AM2.5-C360 model with 5 ensemble members.

The second set of experiments isolates the effect of SST spatial patterns versus globally averaged warming in the future projected period. The first experiment, hereafter referred to as *rcp4.5 flor*, represents a time-varying projected late 21st-century warming scenario, which is run in both

AM2.5-C360 (6 ensembles) and HIRAM (3 ensembles) during the period 2021-2100. AM2.5-C360 and HIRAM use transient RCP4.5 radiative forcings from CMIP5 (Taylor et al. 2012) in these experiments. The SST forcing in this experiment is constructed using observed 2001-2020 climatologies combined with modeled SST anomalies from the FLOR model (Vecchi et al. 2014). FLOR is a fully coupled atmosphere–ocean general circulation model developed at GFDL. The model features an ocean component with an approximately $1^\circ \times 1^\circ$ spatial resolution, and an atmospheric component with the same physics and dynamical core as AM2.5-C360, but run at a lower atmospheric spatial resolution of approximately 50 km. Using the same SST decomposition convention as above, we write the SST forcing of the *rcp4.5 flor* experiment:

$$SST_{\underline{rcp4.5\ flor}} = \underbrace{SST_{clim}(x, y, \text{mon})}_{Observed} + \underbrace{\langle SST' \rangle (t) + SST'(x, y, t)}_{Modeled}, \tag{3}$$

where $SST_{clim}(x, y, \text{mon})$ is the observed 2001–2020 monthly climatology from the bias-corrected SST dataset of (Chan et al. 2021), which is the same observed SST dataset used in the historical *obs sst* and *rm warming* experiments. The use of an observed climatology, rather than the model's simulated climatology, minimizes the impact of model mean-state biases. Both the globally averaged warming anomaly $\langle SST' \rangle (t)$ and the spatially varying anomaly $SST'(x, y, t)$ are derived from the FLOR RCP4.5 projection experiments. As a result, this experiment includes both global mean SST warming and spatially patterned SST changes.

To further isolate the effects of spatially patterned versus globally averaged SST warming on TCs during the future period, we also perform a set of idealized experiments consisting of a control simulation and a perturbed simulation forced by prescribed SSTs. These experiments are described in Hsieh et al. (2020) and Hsieh et al. (2022). In each case, repeating climatological monthly SST patterns are prescribed and held fixed throughout the simulation. All simulations are run for 50 years, such that each experiment experiences 50 repetitions of the same annual SST cycle. First, the control simulation, hereafter named *cntl*, is forced by the observed 1986–2005 average annual SST cycle, where the decomposed SSTs only have an observed climatological component,

$$SST_{cntl} = \underbrace{SST_{clim}(x, y, \text{mon})}_{Observed}. \tag{4}$$

TABLE 1. Controlled experiments used in this study.

Experiment	Period	Climatological Component	Mean Warming Component	Patterned Warming Component
obs sst	1871-2019	Yes, observed	Yes, observed	Yes, observed
rm warming	1871-2019	Yes, observed	No	Yes, observed
rcp4.5 flor	2020-2100	Yes, observed	Yes, modeled	Yes, modeled
cntl	1986-2005	Yes, observed	No	No
2K 2CO2	1986-2005	Yes, observed	Yes, +2K	No

The second idealized experiment, hereafter referred to as *2K 2CO2*, includes the same observed 1986–2005 climatological SST component plus a uniform global mean SST warming of 2 K. The SST forcing for this experiment is therefore

$$SST_{2K\ 2CO2} = \underbrace{SST_{clim}(x, y, \text{mon})}_{Observed} + \langle SST' \rangle, \tag{5}$$

where the global mean warming anomaly $\langle SST' \rangle$ is fixed at +2 K. In addition, atmospheric CO_2 concentrations are doubled relative to the *cntl* experiment in order to represent enhanced greenhouse gas radiative forcing. Differences between the *cntl* and *2K 2CO2* experiments therefore represent the response to a purely global mean SST warming without any change in SST spatial patterns and direct atmospheric effects of increasing carbon dioxide (e.g. Zhao et al. (2009)). By comparing these responses with those obtained from the *rcp4.5 flor* experiment, which includes both global mean warming and spatially patterned SST changes, we can isolate the relative roles of mean versus patterned SST warming in modulating TC activity and its environmental controls.

b. Data

For the historical record of Atlantic tropical cyclone (TC) frequencies from 1871 to 2020, we utilize the adjusted dataset developed by Vecchi and Knutson (2008). To compute observed seasonal large-scale environmental factors, we use the ERA5 reanalysis dataset (Hersbach et al. 2020) during the period 1979–2020 and the MERRA2 reanalysis dataset (Gelaro et al. 2017) during the period 1980-2020.

c. TC and seed tracking

To track tropical cyclones (TCs), we employ the algorithm developed by Harris et al. (2016), setting the specific thresholds for wind speed, minimum sea level pressure, lifetime, and warm-core characteristics as in Chan et al. (2021). The algorithm utilizes the following 6-hourly inputs: sea level pressure, 850 hPa vorticity, 10-m wind speed, and mid-tropospheric (300–500 hPa) air temperature. The process begins by searching for local minima in sea level pressure and then applying an 850 hPa vorticity threshold of $1.5 \times 10^{-4} \mathrm{s}^{-1}$, which filters out disorganized or weak systems. For the remaining storms, additional filters ensure longevity and robustness, including a minimum total lifetime of 72 hours (Villarini et al. (2011a)), at least 48 hours with a warm core (defined as a maximum 300–500 hPa temperature encircled by a 2° contour within 500 km of the storm's minimum sea level pressure), and at least 36 consecutive hours with both a warm core and maximum 10-m winds exceeding 15 m s^{-1}. We require that at least one time step along the storm's trajectory that the maximum wind speed exceeds 17 m s^{-1}.

For the HIRAM model, we implemented minor modifications to the algorithm to ensure that the tracked TC frequency in the reference experiment closely matches the globally averaged TC frequency. These are the same adjustments for HIRAM are used in Yang et al. (2021). The warm-core temperature contour is increased from 2 to 2.5° and the required proximity of the warm core to the storm center is decreased from 500 km to 110 km. For the AM2.5-C360 model, we retain the original thresholds without modifications.

Seed detection is performed using the aforementioned TC tracking algorithm, with the approach described in Yang et al. (2021). We examine candidate points as local pressure minimal that exceed the a $1.5 \times 10^{-4} \mathrm{s}^{-1}$ vorticity threshold. A seed must span a radius of at least 50 km and exhibit a maximum 850 hPa relative vorticity of at least $4 \times 10^{-4} \mathrm{s}^{-1}$ during its lifetime. The seed tracking algorithm remains unchanged for both atmospheric models.

d. Seed and probability indices

We use Hsieh et al. (2020)'s probabilistic framework, which decomposes annual TC counts into two stages: precursor seed disturbances and fully developed TCs. Based on these two stages, Hsieh et al. (2020) infer that the annual frequency of North Atlantic TCs, N_{TC} follows a binomial

distribution:

$$N_{TC} \sim \text{binom}(N_s, P), \tag{6}$$

where N_s is the total number of first stage rotating seeds present in the basin for a given year, which has units of storm count, and P is the dimensionless basin-aggregated probability that a first-stage seed transitions into a second-stage TC. Consequently, the expected value of N_{TC}, which has dimensions of storm count, is given by

$$N_{TC} = N_s \times P. \tag{7}$$

For instance, if a given season produces 75 seeds ($N_s = 75$), of which 15 transition into TCs ($N_{TC=15}$), the basin-aggregated empirical transition probability from the first stage to the second stage for that season would be $P = 15/75 = 0.2$.

Hsieh et al. (2020)'s ansatz parametrizes N_s and P as functions of large-scale environmental conditions. First, they develop a proxy for N_s, known as the seed propensity index (SPI):

$$N_s \approx SPI = (\kappa) \cdot (-\omega) \cdot \frac{1}{1 + Z^{-1/\sigma}}, \tag{8}$$

where κ is a constant proportionality fitted parameter in units of storms per Pa s^{-1}, ω is the monthly mean 500 hPa vertical velocity in pressure coordinates (in units of Pa s^{-1} where $\omega > 0$ is for downward motion), $\sigma = 0.69$ is a constant nondimensional fitting parameter, and Z is nondimensional parameter that represents the ability of the low-level vorticity to spinup and is a function of low level vorticity (Ikehata and Satoh (2021)),

$$Z = \frac{f + \zeta}{\sqrt{|\beta + \partial_y \zeta| U}}, \tag{9}$$

where f represents the Coriolis parameter and β represents its meridional gradient, ζ is the monthly mean relative vorticity at 850 hPa, and U is assumed to be a constant wind speed of 20 m/s which is empirically fit using aquaplanet model simulations.

Next, the probability that a weakly rotating seed develops into a strongly rotating TC (P; a dimensionless value between 0 and 1) is parameterized as a probability index ($P(\Lambda)$):

$$P \approx P(\Lambda) = \frac{1}{1 + (\Lambda_0/\Lambda)^{1/\gamma}}, \tag{10}$$

where $\Lambda_0 = 0.014$ and $\gamma = -0.9$ are constant dimensionless fitting parameters, and Λ is the ventilation index defined by Tang and Emanuel (2010) and Tang and Emanuel (2012), which measures the degree to which the influx and circulation of cold dry air into the storm's convective plume can inhibit the storm's strength. The ventilation index is a non-dimensional metric:

$$\Lambda = \frac{\nu_s \cdot \chi}{PI}, \tag{11}$$

where ν_s is the vertical wind shear between 850 hPa and 250 hPa in units of m s^{-1}, PI is potential intensity (the theoretical upper limit of a TC's wind speed based on temperature contrasts between the sea surface and upper troposphere in units of m s^{-1}), and χ is a dimensionless parameter representing moist entropy deficit. This parameter is defined as

$$\chi = \frac{s_m^* - s_m}{s_0^* - s_b}, \tag{12}$$

where s_m^* is the saturation moist entropies at 600 hPa in the inner core of a TC, s_m is the environmental entropy at 600 hPA, s_0^* are the saturation moist entropy at the sea surface, and s_b is the entropy of the boundary layer. The numerator of the ventilation index equation (11) represents the difference in midlevel entropy between the TC and its environment, while the denominator represents the air-sea disequilibrium.

Thus, equations (8) and (10) serve as proxies for N_s and P expressed as functions of large-scale environmental factors that can be derived from climate model simulations. This framework offers a valuable approach for studying TCs using climate models, particularly those that lack the spatial resolution required to directly resolve TCs and seeds. We compute the mean Atlantic basin SPI over 5–30°N and $P(\Lambda)$ over 10–30°N. The slightly more equatorward bound for the SPI index reflects the sequential nature of TC development: storms first emerge as precursor disturbances before transitioning into fully developed TCs. Because the TC main development region, where

most Atlantic TCs reach full maturity, is typically defined north of 10°N (Vecchi et al. 2011)), extending the SPI domain southward to 5°N accounts for precursor seed formation that occurs prior to TC genesis. Our results are not qualitatively sensitive to this choice, as using a 10–30°N domain for both SPI and $P(\Lambda)$ yields similar conclusions. Following the methodology of Vecchi et al. (2019), we compute the TC framework and evaluate the monthly large-scale environmental controls on Atlantic TC activity during the climatologically most active portion of the season, June–November.

3. Results

a. Evaluating the models for historical Atlantic TCs

First, we assess how well the historical simulations (*obs sst* and *rm warming*) reproduce past observed TC variability. Figure 1a compares observed annual Atlantic TC counts to those simulated by both models. Overall, the *obs sst* simulation in both models and AM2.5-C360 *rm warming* simulation effectively capture interannual fluctuations in TC activity. For instance, all simulations show a local peak in 2005 and a trough in 1982, corresponding to historically active and inactive years, respectively. The annual ensemble-mean correlation between simulated *obs sst* record and observed TC frequency, without detrending the record, is slightly higher in AM2.5-C360 compared to HIRAM, though both exhibit similar values (~0.5). Interestingly, the annual ensemble-mean correlation between simulated *rm warming* record and observed TC frequency is slightly higher ($r = 0.6$) than that for the *obs sst* simulations.

For most years, observed TC fluctuations (black line) remain within the 95% inter-ensemble spread of all model simulations (blue, orange, and green shading), suggesting that the model simulations reproduce realistic levels of TC variability. However, the exceptionally active 2020 season, and several seasons immediately preceding it, are not well captured, with observed TC counts lying outside the estimated 95% confidence interval of both models. The observed TC count also lies outside the estimated 95% confidence interval in other years, such as 1890, 1916, 1933, and 1982. Work is better underway to better understand the extent to which this discrepancy, which represents a deficiency in the models or the forcing, is due to ambiguity in the observed target or is likely to be best understood as one of the unlikely outcomes that even a well-calibrated system will exhibit.

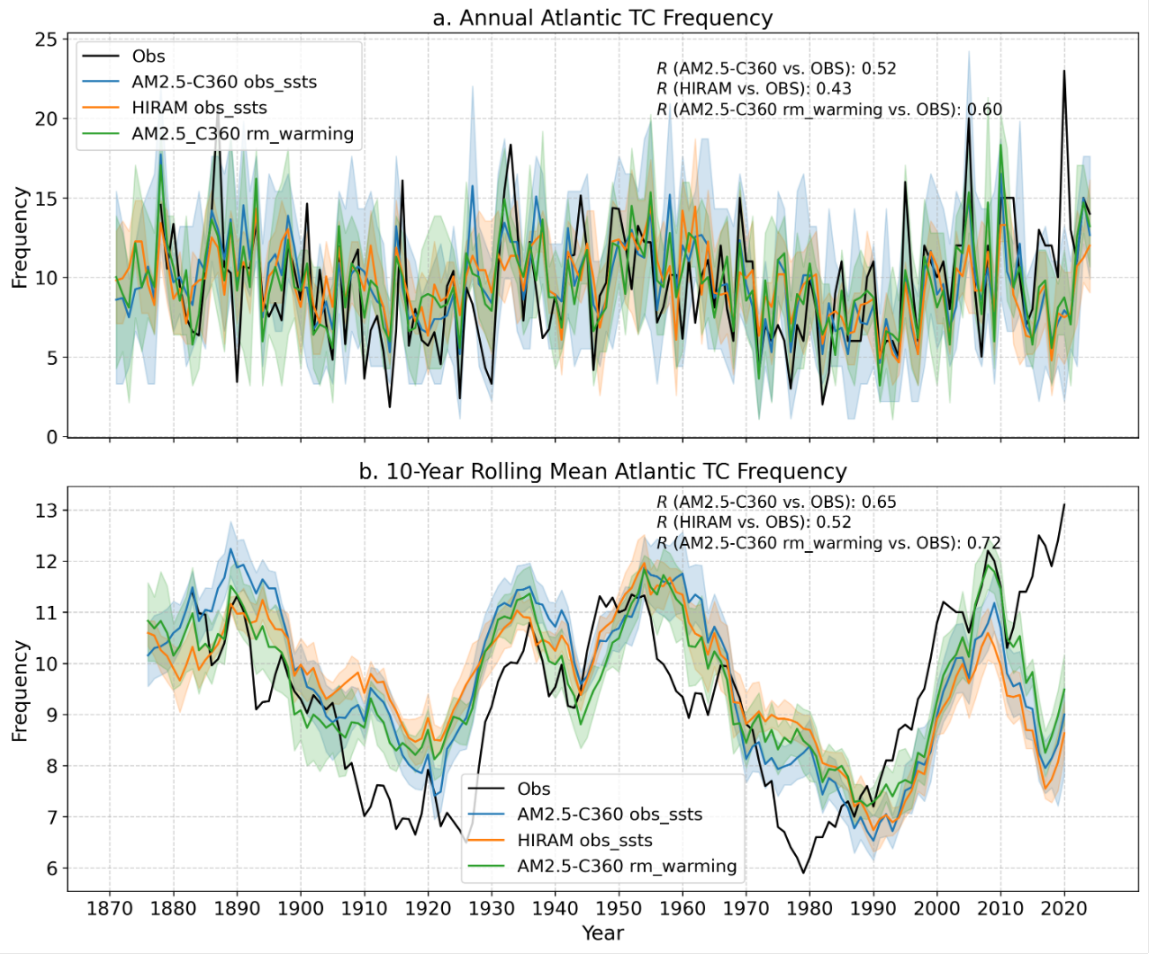

294 FIG. 1. (a) Annual TC frequency from 1871 to 2023, including the adjusted observational record from Vec-
295 chi and Knutson (2011) (black), AM2.5-C360 obs_sst simulation (blue), AM2.5-C360 rm_warming simulation
296 (green), and HIRAM obs_sst simulation (orange). The shading represents the ensemble minimum and maximum
297 values for each simulation. (b) Ten-year rolling mean of the TC frequency shown in (a). Solid lines indicate
298 ensemble means, while shaded regions represent the bootstrapped 95% confidence intervals derived from re-
299 sampling ensemble members. Confidence intervals are obtained by computing the 10-year rolling mean for
300 each ensemble member, resampling the ensemble with replacement 1,000 times, and taking the 2.5th and 97.5th
301 percentiles of the resulting distribution, which are represented by the bounds of the shading.

312 We propose several hypotheses for this model–observation discrepancy. First, aerosol changes
313 during this period may not have been fully represented in the SST-forced simulations. The onset
314 of the COVID-19 pandemic in early 2020 sharply reduced global travel and industrial activity,

potentially lowering aerosol emissions or changing their geographic distribution. At the same time, new International Maritime Organization regulations, effective January 1, 2020, reduced the sulfur content of shipping fuels from 3.5% to 0.5%. While intended to improve air quality and public health, this reduction diminished marine aerosol loading, brightening fewer clouds and decreasing reflected solar radiation. The resulting radiative imbalance likely accelerated short-term warming, creating atmospheric conditions more favorable for TC development (Diamond 2023; Jordan and Henry 2024; Zhang et al. 2025), yet this signal should be constrained in the observed SST forcing. Still, such effects cannot account for the discrepancies observed in the years immediately prior to 2020.

Additional possible causes include model and storm-tracking limitations within AM2.5-C360 and HIRAM, as well as evolving observational practices since the advent of the satellite era. For example, modern satellites may have become increasingly capable of detecting weaker disturbances, inflating the observed storm record relative to earlier periods. Finally, internal climate variability and random weather fluctuations may also have played a role (e.g. Kortum et al. (2024)). A fuller exploration of these hypotheses lies beyond the scope of this report but remains an important direction for future research.

Figure 1b evaluates the ability of the model simulations to reproduce historical low-frequency variability in Atlantic TC activity using a 10-year rolling mean. This filtering suppresses interannual variability while retaining a combination of decadal (10–20 year) and multidecadal (30+ year) variability. The *obs sst* simulations in both models, as well as the AM2.5-C360 *rm warming* simulation, broadly reproduce the observed low-frequency fluctuations in Atlantic TC activity since the late nineteenth century. In particular, these simulations capture decadal-scale peaks in the 1930s and 1950s and a relative minimum during the early twentieth century (1910–1930). They also reproduce multidecadal variations, including elevated activity during 1871–1900 and 1930–1970 and reduced activity during 1900–1930 and 1970–2000.

A key exception is the models' inability to reproduce the recent decadal-scale increase in TC activity from 2010–2020. During 2010–2018, the simulated and observed 10-year rolling-mean TC counts exhibit a pronounced anticorrelation: the observations show increasing decadal-mean activity, whereas all three model simulations display a decline over the same period. Although discrepancies between simulated and observed interannual TC counts are also evident during

2015–2019 (Fig. 1a), we attribute the decadal-scale anticorrelation primarily to the models' failure to capture the exceptionally active 2020 hurricane season, as discussed above. The 2020 season was anomalous, producing 23 named storms, whereas the ensemble-mean simulations generate approximately eight storms. This extreme observed outlier likely inflates the observed 10-year rolling mean trend over 2010–2020, while the comparatively weak simulated activity in 2020 contributes to a declining trend in the modeled decadal means.

Consistent with the annual analysis, the ensemble spread for the 10-year rolling mean TC record is larger in the AM2.5-C360 *obs sst* simulation than in the HIRAM *obs sst* simulation, reflecting the larger ensemble size in AM2.5-C360 (ten members) compared to HIRAM (five members). Notably, correlation coefficients for the 10-year rolling mean TC counts are modestly higher than those obtained for annual TC frequencies, indicating improved model performance at capturing decadal-scale variability. The correlations between observed and simulated 10-year rolling mean TC counts are higher for AM2.5-C360 ($r = 0.65$ and $r = 0.72$) than for HIRAM *obs sst* ($r = 0.52$), suggesting greater skill in AM2.5-C360 for reproducing decadal Atlantic TC variability.

In both Fig. 1a and Fig. 1b, the strongest agreement between observed TC counts and the simulated ensemble mean occurs in the AM2.5-C360 *rm warming* simulation. Importantly, this experiment closely reproduces the decadal and multidecadal variability evident in the observational record, and its variability is nearly indistinguishable from that of the *obs sst* simulations. These results suggest that historical TC variability is primarily driven by the spatial pattern of ocean warming rather than the global-mean warming trend, as the *rm warming* simulation closely matches the *obs sst* simulation despite the removal of the mean warming signal.

b. Mean warming versus patterned warming

In this section we discuss the effect of regional warming patterns versus global mean warming on Atlantic TCs and their environmental controls during both the historical and projected record, leveraging all these experiments described in Section 2.

(i) Historical record

First, Fig. 1 indicates that regional sea surface temperature (SST) patterns, rather than the global-mean warming trend, primarily drove interannual, decadal, and multidecadal variability in Atlantic

tropical cyclone (TC) activity during the historical period. This inference follows from the strong similarity between the AM2.5-C360 *obs sst* and *rm warming* simulations, both of which exhibit comparable TC variability and moderate correlations with the observed TC record. Because the sole difference between these simulations is the removal of the global-mean SST warming trend in the *rm warming* experiment, any systematic divergence between the two would be attributable to mean warming. The absence of such divergence therefore suggests that historical TC variability cannot be explained by the global-mean warming trend alone and instead reflects the influence of regional SST patterns.

To further assess whether regional SST patterns drive historical variability in the large-scale environmental controls on TCs, we examine the two components of the TC proxy proposed by Hsieh et al. (2020), SPI and $P(\Lambda)$, across three simulations: the *obs sst* simulations in both models and the AM2.5-C360 *rm warming* simulation. Figure 2 shows 10-year rolling mean time series of basin-averaged SPI and $P(\Lambda)$ for these simulations over the historical period. Substantial differences between the *rm warming* and *obs sst* simulations would indicate a role for global-mean warming in modulating the environmental controls on TC activity.

We find that AM2.5-C360 and HIRAM exhibit systematic differences in the mean magnitudes of SPI and $P(\Lambda)$. In particular, $P(\Lambda)$ is consistently higher in both AM2.5-C360 simulations than in HIRAM by approximately 0.1, whereas SPI is lower in AM2.5-C360 by about 1.5×10^{-3}. Despite these mean offsets, SPI exhibits no persistent long-term trend in any simulation. Instead, SPI is dominated by pronounced multidecadal (30–60 yr) variability, with elevated values during 1880–1910 and 1930–1970 and reduced values during 1910–1930 and 1970–2000. In contrast, $P(\Lambda)$ displays a markedly different low-frequency evolution. While superimposed with decadal (10–20 yr) fluctuations, including relative maxima in the 1890s, 1950s, 1970s, and 2000–2020 and a minimum during 1910–1930, $P(\Lambda)$ is characterized by a gradual decline over much of the historical period. Most notably, we observe a pronounced multidecadal decrease in $P(\Lambda)$ between approximately 1960 and 1990.

Crucially, the time series of both SPI and $P(\Lambda)$ are nearly identical between the AM2.5-C360 *obs sst* and *rm warming* simulations, with their 95% confidence intervals overlapping for almost the entire record. This close agreement demonstrates that the historical variability of the large-scale environmental controls on Atlantic TC activity is governed primarily by regional SST patterns

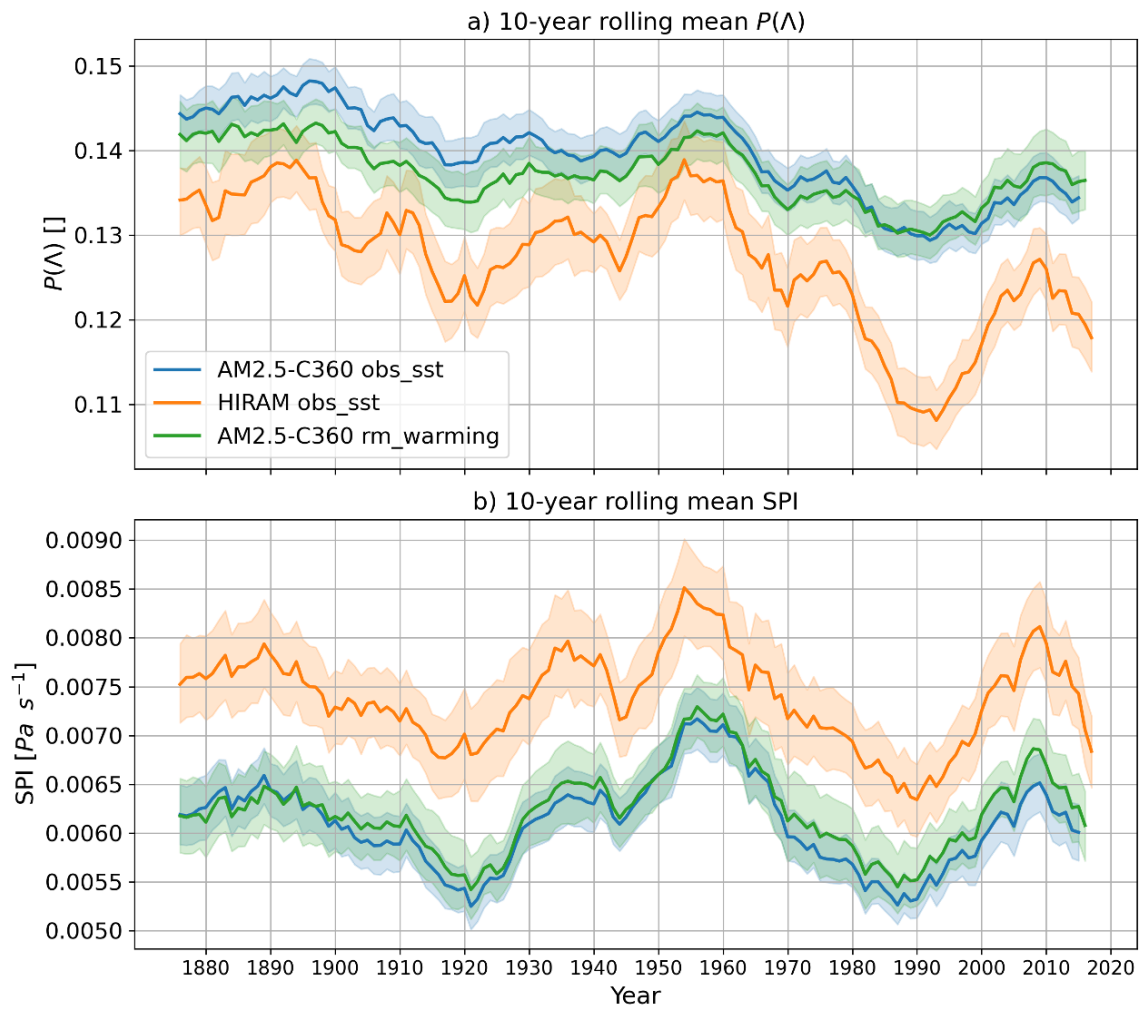

408 FIG. 2. 10-year rolling mean of a) $P(\Lambda)$ and b) SPI, from the AM2.5-C360 *obs sst* simulation (blue), the
409 AM2.5-C360 *rm warming* simulation (green) and the HIRAM *obs sst* simulation (orange) during the 1871-2020
410 historical period. Shaded regions indicate the bootstrapped 95% confidence intervals as in Fig. 1, derived from
411 resampled ensemble members, while solid lines represent the ensemble means.

404 rather than by the global-mean warming trend. The similarity of these proxy components in
405 simulations with and without mean warming reinforces the conclusion that spatial SST structure,
406 rather than uniform warming, dominated TC-relevant environmental variability over the historical
407 period.

412 *(ii) Projected record*

413

To evaluate the relative roles of regional SST patterns and global-mean warming in shaping future Atlantic tropical cyclone (TC) activity and its environmental controls, we analyze the sensitivity of both annual TC counts and the TC proxy ($SPI \times P(\Lambda)$) to mean SST warming across two experimental frameworks in both models. Specifically, we examine sensitivities in the *rcp4.5 flor* simulations, which include both patterned and mean SST warming, and contrast them with sensitivities derived from the idealized comparison between the *cntl* and *2K 2CO2* experiments, which isolate the response to a spatially uniform +2 K global-mean warming. Because the *rcp4.5 flor* simulations incorporate both components of warming, whereas the *2K 2CO2*–*cntl* comparison reflects only the effect of global-mean warming, systematic differences in TC and TC-proxy sensitivities between these two cases can be attributed to the influence of regional SST patterns. Accordingly, large discrepancies between the sensitivities diagnosed from the *rcp4.5 flor* simulations and those from the idealized uniform-warming experiments indicate that, during the future projected period, variability in Atlantic TC activity is governed primarily by regional SST patterns rather than by global-mean SST warming alone.

Figure 3 shows the sensitivity of Atlantic tropical cyclone (TC) counts to global-mean SST warming relative to the 1986–2005 climatology. We first note that the sign and magnitude of the diagnosed sensitivities differ across models, even for the same experimental configurations. In the AM2.5-C360 uniform-warming experiments, based on the comparison between the *2K 2CO2* and *cntl* simulations, no statistically robust increase or decrease in Atlantic TC counts is evident in response to uniform global-mean warming. In contrast, the corresponding HIRAM experiments yield a negative sensitivity of approximately -1.5 to -2 TCs per K, indicating a projected decline in TC activity under uniform warming in that model. Model-dependent differences are also apparent in the *rcp4.5 flor* simulations, which include both mean and patterned SST warming. In AM2.5-C360, these simulations indicate a modest positive sensitivity of roughly +0.5 to +1.5 TCs per K, suggesting a slight increase in TC activity with warming. By contrast, the HIRAM *rcp4.5 flor* simulation exhibits a wide range of sensitivities, spanning approximately -1.0 to +2.3 TCs per K, with no consistent sign. The substantial discrepancies between models highlight the considerable uncertainty in projections of future Atlantic TC activity in response to SST warming.

For each model, comparisons of TC sensitivity to mean warming between experiments that include regional patterned warming (*rcp4.5 flor*) and those that exclude it (*cntl* and *2K 2CO2*)

reveal pronounced differences in both the sign and magnitude of the projected response. In the AM2.5-C360 controlled experiments without patterned warming, TC sensitivity to mean warming is not statistically distinguishable from zero. In contrast, the AM2.5-C360 experiment that includes patterned warming exhibits a clear positive sensitivity of TC activity to mean warming. A similar contrast emerges in HIRAM: the controlled experiments without patterned warming show a robust negative sensitivity of TC activity to mean warming, whereas the experiment that includes patterned warming displays no consistent trend. These sign reversals between experiments with and without regional SST patterns indicate that patterned warming, rather than global-mean warming alone, plays a dominant role in shaping projected Atlantic TC variability.

We next examine the sensitivity of the TC proxy ($SPI \times P(\Lambda)$) to mean warming in simulations that do and do not include regional patterned warming in both AM2.5-C360 and HIRAM (Fig. 3b). Consistent with the TC count results, we find substantial differences in proxy sensitivity between experiments with and without patterned warming. In AM2.5-C360, both experimental configurations show a decrease in the TC proxy with increasing mean warming; however, the magnitude of this sensitivity is nearly twice as large in the uniform-warming experiment compared to the experiment that includes patterned warming. In HIRAM, the sign of the proxy sensitivity differs between experiments. The uniform-warming experiment exhibits a decrease in the TC proxy with mean warming, whereas the experiment that includes patterned warming shows no clear trend. Together, these results indicate that regional SST patterns exert a critical influence on the large-scale environmental controls of future Atlantic TC activity, beyond the effect of global-mean warming alone.

Finally, we find that the simulated sensitivities of TC counts and the TC proxy are consistent in HIRAM but diverge in AM2.5-C360. In HIRAM, the uniform-warming experiment shows a decrease in TC counts with increasing mean warming, accompanied by a corresponding decrease in the TC proxy. Likewise, in the experiment that includes both mean and patterned warming, where TC counts exhibit no clear sensitivity to mean warming, the TC proxy also shows no discernible trend. This internal consistency suggests that, in HIRAM, the proxy reliably reflects the model's simulated TC response to warming. In contrast, AM2.5-C360 exhibits a mismatch between TC count and proxy sensitivities. In the uniform-warming experiment, TC counts show no statistically robust response to mean warming, whereas the TC proxy indicates a declining sensitivity. Con-

versely, in the experiment that includes both patterned and mean warming, TC counts exhibit a positive sensitivity to mean warming, while the TC proxy indicates a negative response. Although the TC proxy in the AM2.5-C360 *rcp4.5 flor* simulation remains positively correlated with the projected TC count time series (Fig. 4), this discrepancy suggests a systematic bias in the proxy's representation of the mean response during the future projection period. Nonetheless, the proxy continues to capture the decadal variability of TC activity, indicating that the bias primarily affects the mean trend rather than the temporal variability. We further explore the ability of the TC proxy to capture TC variability throughout the past and projected record in the following section.

c. TC seed and probability proxies and environmental controls

In this section, we evaluate the extent to which the seed-probability framework ($SPI \times P(\Lambda)$) captures TC variability in our temporally varying simulations during both the historical and projected periods using the *obs sst* and *rcp4.5 flor* experiments. Due to the similarity in results between the *obs sst* and *rm warming* experiments, we only include the results from the *obs sst* experiment. First, in Section a, we demonstrate that the SPI framework faithfully reproduces both the spatial climatology and temporal variability of tracked TC seeds. This agreement provides confidence in applying the full theoretical framework, $SPI \times P(\Lambda)$, to approximate TC counts.

Next, to evaluate the full theoretical framework, we examine the correlation between the parametrized TC estimate ($SPI \times P(\Lambda)$) and the simulated TCs from the models. It is important to note that the proxies SPI and $P(\Lambda)$ are not independent variables, but exhibit a spatial-temporal covariation (Fig. A3). Visual inspection of Figure 4 indicates that the framework captures key features of low-frequency TC variability, encompassing decadal (10–20 yr) and multidecadal (30–60 yr) timescales, in both models during the historical and projected periods. In particular, the framework reproduces decadal-scale maxima in TC activity during the 1930s, 1950s, 2000–2010, 2020s, 2040–2055, and 2060–2075, as well as decadal-scale minima around 1920, 1980–2000, 2040, and 2060. In addition, the framework captures a pronounced multidecadal decline in TC activity from approximately 1955 to 1990.

In both observed and projected periods, the parametrized TCs remain within the 95% confidence interval of the simulated TCs, indicating that the framework provides a realistic representation of TC variability. However, when comparing model performance, the framework exhibits stronger

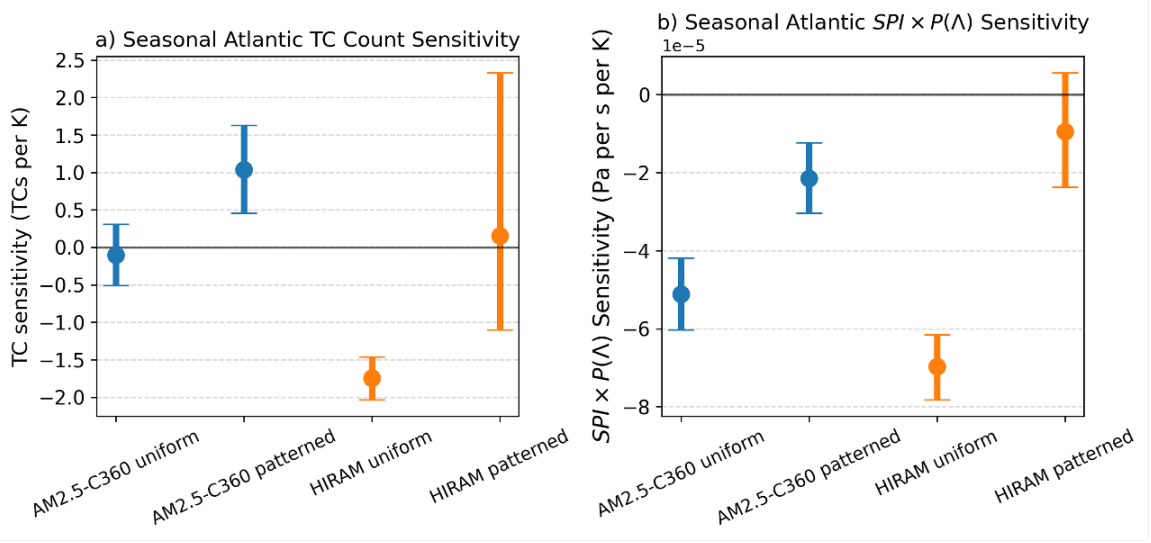

FIG. 3. Sensitivity of (a) Atlantic tropical cyclone (TC) counts and (b) the Atlantic TC proxy ($SPI \times P(\Lambda)$) to mean warming across experiments with and without patterned SST warming during the future projection period. AM2.5-C360 experiments are shown in blue and HIRAM experiments in orange. Experiments labeled "uniform" on the x-axis represent TC sensitivity to uniform mean warming, computed by comparing the *cntl* and *2K 2CO2* experiments. Sensitivity is calculated as the difference in TC counts or proxy values between the *2K 2CO2* and *cntl* simulations, divided by 2 to account for the imposed +2 K warming. The bars denote 95% confidence intervals estimated via bootstrapping. For the uniform experiments, confidence intervals are obtained by randomly pairing one year from the *cntl* experiment and one year from the *2K 2CO2* experiment (each consisting of 50 years of identical forcing), repeating this procedure 1,000 times without replacement, and computing the 2.5th, mean, and 97.5th percentiles of the resulting sensitivity distribution. Experiments labeled "patterned" represent TC sensitivity to mean warming in the *rcp4.5 flor* simulations. Because this experiment is transient rather than idealized, sensitivity is estimated by regressing seasonal Atlantic TC counts (or proxy values) against seasonal mean warming relative to the 1986–2005 climatology. Confidence intervals are obtained by bootstrapping the ensemble-member regression slopes 1,000 times with replacement and extracting the 2.5th and 97.5th percentiles. In both panels, the lower bound of each bar corresponds to the 2.5th percentile, the central marker denotes the bootstrap mean, and the upper bound indicates the 97.5th percentile.

agreement with HIRAM than AM2.5-C360, as reflected in the higher correlation coefficient between parametrized and simulated ensemble mean TC count (0.94 vs. 0.78). In AM2.5-C360, the framework systematically underestimates projected TC activity, a behavior consistent across both

the uniform and patterned warming experiments shown in Figure 3. Overall, these results indicate a smaller bias between tracked TCs and the TC proxy in HIRAM than in AM2.5-C360 during the projected period.

Next, we assess the variability of SPI and $P(\Lambda)$ in both the historical and projected records. Figure 5 illustrates the temporal evolution of SPI and $P(\Lambda)$ across the entire combined record in both models' *obs sst* and *rcp45 flor* experiments. As we observe in Figure 2, the models exhibit distinct magnitudes of SPI and $P(\Lambda)$, with $P(\Lambda)$ higher in AM2.5-C360 than in HIRAM, while SPI remains lower in AM2.5-C360. The magnitudes of these variables remain distinct throughout the historical and projected record. Examining SPI in Figure 5b, we find no discernible long-term trend but rather multidecadal and decadal variability. As shown in Figure 2b, during the historical period (1871–2019), SPI displays prominent multidecadal fluctuations, with peaks from 1880-1910 and 1930-1970 and reduced values from 1910-1930 and 1970-2000. In contrast, the projected record reveals predominantly decadal variability, characterized by peaks recurring approximately every 20 years. Meanwhile, $P(\Lambda)$ follows a distinct pattern: during the historical period, it exhibits a steady decline, most pronounced 1960 to 1990 (Figure 2), before stabilizing in the projected record, where variability remains relatively stagnant, except for one period of elevated values around 1970. The most striking trend in the entire record for both SPI and $P(\Lambda)$ is a is a sharp decline from 1960 to 1990, followed by a notable rebound and increase from 1990 to 2010.

(i) Thermodynamic variables

To understand why $P(\Lambda)$ exhibits a decreasing trend throughout the historical period but remains relatively stable in the projected period, we examine its thermodynamic components, χ and PI, both of which respond directly to anthropogenic warming. Figure 6 illustrates the relationship between PI and χ^{-1} in both the *obs sst* and *rcp4.5 flor* experiments, as well as in several reanalysis datasets. During the historical period (blue) and across the duration of the reanalysis data (orange and olive), we observe a direct relationship between PI and χ^{-1}, indicating that their effects compounded each other. When PI was higher and more conducive to TCs, χ was lower, further enhancing storm activity. In contrast, during the projected period (green), this relationship reverses: as one variable becomes more favorable for TC activity, the other becomes less favorable, suggesting that their effects offset each other. Additionally, the models exhibit distinct magnitudes of PI and χ^{-1}. PI is notably higher in HIRAM by approximately 7 m s^{-1}. While PI values in HIRAM are closer to

those found in reanalysis products, they still fall short by about 5 m s^{-1}. Meanwhile, χ^{-1} is slightly higher in AM2.5-C360 than in HIRAM, though the reanalysis datasets display significant variation in their projections of χ^{-1}.

To further investigate the reversal of the relationship between χ and PI in the historical and projected periods, we plot their time series in Figure 7. The results show that χ increases consistently throughout the entire record, in addition to some decadal variability, suggesting that anthropogenic warming enhances the moisture deficit between the storm's inner core and its environment. Meanwhile, the trend lines in Figure 7 reveal that on top of some decadal fluctuations, PI decreases throughout most of the historical period, from 1871 to roughly 1980, but increases after 1980 throughout the rest of the projected period. This shift in the sign of the PI trend around 1980 is the primary driver of the observed reversal in the PI and χ relationship.

To better understand the discrepancy between observed and projected trends in PI, we analyze trends in tropical sea surface temperatures (SSTs) during both periods. Tropical SSTs exert a strong influence on upper-tropospheric temperatures, which in turn regulate PI (Emanuel et al. (2013); Eusebi et al. (2025); Ramsay and Sobel (2011); Vecchi and Soden (2007); Vecchi et al. (2013)), since PI is fundamentally determined by the temperature contrast between the surface and the upper troposphere. The primary mechanism linking SSTs to free-tropospheric temperatures is deep convection (Flannaghan et al. (2014); Fueglistaler et al. (2015); Sobel et al. (2002)), which is most vigorous in regions of the warmest tropical SSTs (Zhang (1993)). Consequently, the warmest tropical SSTs, typically associated with the western Pacific warm pool, effectively set upper-tropospheric temperatures across the tropics through convective adjustment.

In the present climate, Sobel et al. (2002) showed that the tropical-mean SST is closely tied to the warmest tropical SSTs. Thus, the rate at which local SSTs warm relative to the tropical-mean warming rate provides a key indicator of PI. Motivated by this framework, we compare Atlantic TC-season SST warming rates with those of the broader tropics during both the observed (Fig. 8) and projected (Fig. 9) periods. Although the tropical Atlantic warmed during the historical period (Fig. 8a), it did so more slowly than the tropical mean (Fig. 8b). In contrast, in the projected period, tropical Atlantic SSTs are expected to warm not only in absolute terms but also more rapidly than the tropical mean. These results imply that the Atlantic surface-to-troposphere temperature contrast weakened in the historical record but is projected to strengthen in the future. We therefore

propose that the observed decline in PI, versus its projected increase, arises from differences in relative SST changes. In particular, the spatial pattern of Atlantic SST warming relative to the tropics plays a central role in shaping PI trends and their linkage to χ, both of which are critical drivers of changes in $P(\Lambda)$.

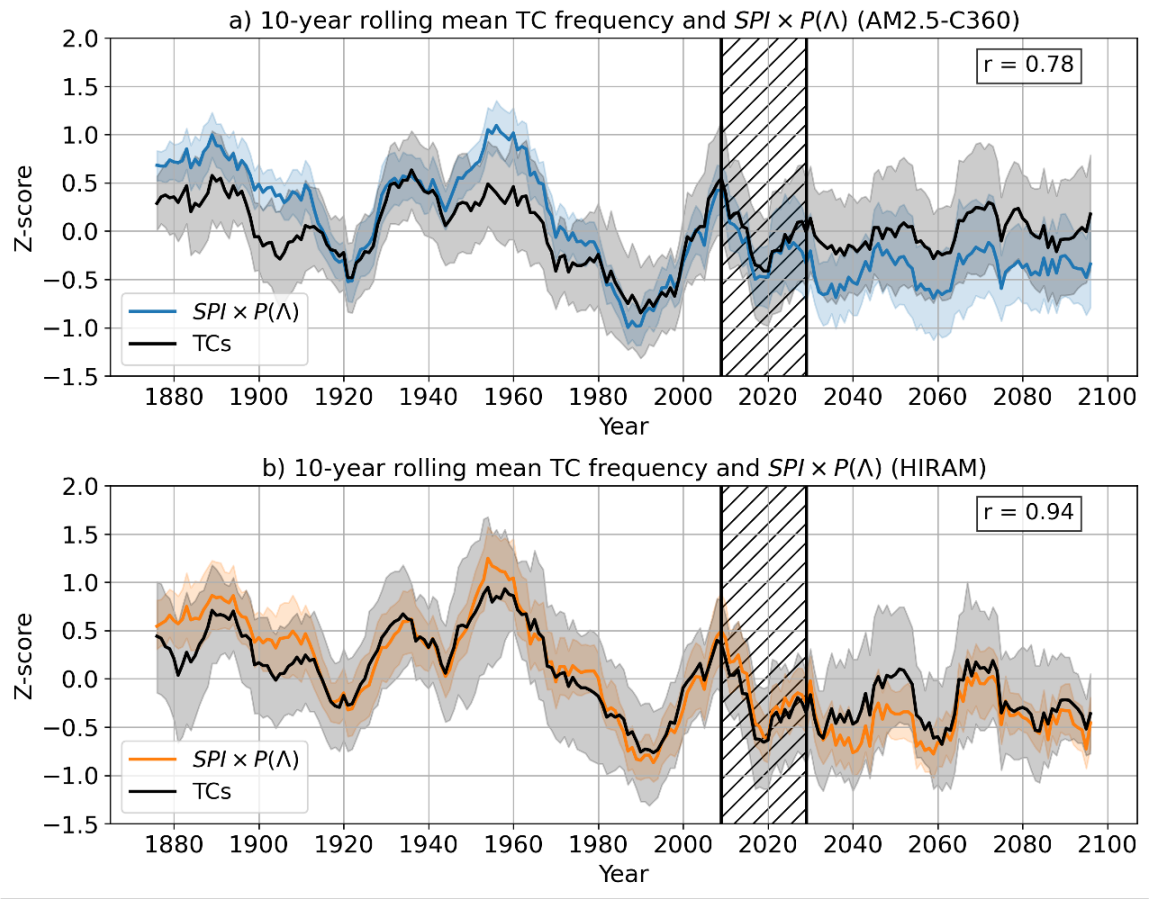

FIG. 4. Normalized 10-year rolling mean of simulated Atlantic tropical cyclone (TC) frequency (N_{TC}; black) and parameterized TC frequency (SPI $\times P(\Lambda)$; colored) for (a) AM2.5-C350 (blue) and (b) HIRAM (orange). Shaded regions indicate the bootstrapped 95% confidence intervals as in Fig. 1, derived from resampled ensemble members, while solid lines represent the ensemble means. The historical period (1871–2019) is based on the *obs SST* simulation, whereas the future period (2020–2100) is derived from the *rcp4.5 SST* simulation. These two periods are combined into a continuous time series, with both simulated and parameterized TC frequencies standardized using a Z-score normalization: $Z(x) = (x - \mu_x)/\sigma_x$, where x represents the data point, μ_x is the mean, and σ_x is the standard deviation over the full record. Correlation coefficients between the ensemble mean simulated and parameterized TC frequencies are displayed in the top right corner of each panel. Values to the left of the hatched region correspond to simulations forced with observed SSTs (*obs sst*), while values to the right correspond to simulations forced with observed climatology plus projected SST patterns (*rcp45 flor*). The hatched region marks a smooth transition that blends both forcing regimes.

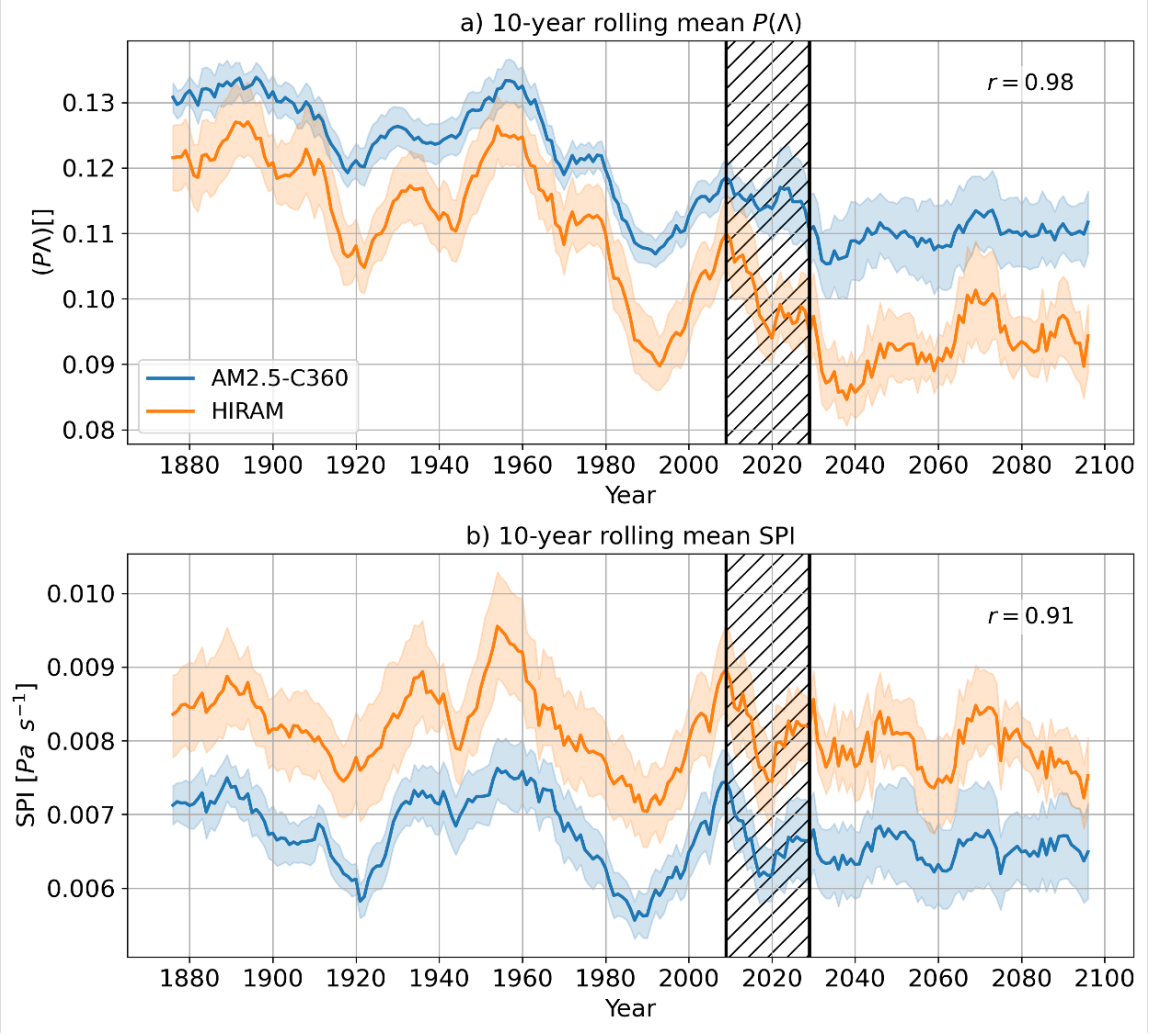

552 FIG. 5. 10-year rolling mean of a) $P(\Lambda)$ and b) SPI, from AM2.5-C360 (blue) and HIRAM (orange). Shaded
553 regions indicate the bootstrapped 95% confidence intervals as in Fig. 1, derived from resampled ensemble
554 members, while solid lines represent the ensemble means. The historical period (1871–2019) is based on the
555 *obs SST* simulation, whereas the future period (2020–2100) is derived from the *rcp4.5 SST* simulation. These two
556 periods are combined into a continuous time series. The correlation coefficients between the ensemble mean of
557 each model is shown in the upper right corner of each panel. Values to the left of the hatched region correspond to
558 simulations forced with observed SSTs (*obs sst*), while values to the right correspond to simulations forced with
559 observed climatology plus projected SST patterns (*rcp45 flor*). The hatched region marks a smooth transition
560 that blends both forcing regimes.

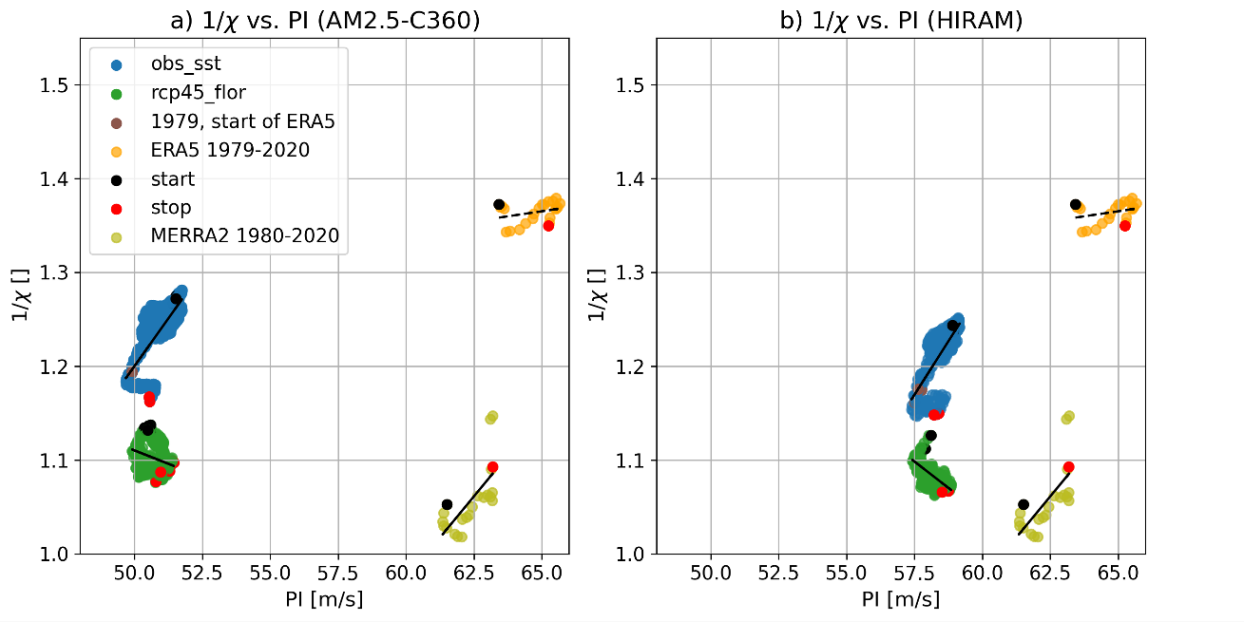

FIG. 6. 10-year rolling mean of TC-season basin-averaged χ^{-1} and PI for (a) AM2.5-C360 and (b) HIRAM. To clarify their relationship, both axes are oriented so that increasing values indicate more favorable conditions for TC activity. Blue and green dots represent historical (1871–2019) and projected (2020–2100) periods, and the *obs sst* and *rcp4.5 flor* experiments, respectively, while orange and olive dots correspond to ERA5 (1979–2020) and MERRA5 (1980–2020) reanalysis data. Black and red dots denote the start and end of each period. Trend lines are plotted for each period, with solid lines indicating statistically significant trends ($p < 0.05$) and dashed lines otherwise. Positive (negative) trends indicate periods where PI and χ effects reinforce (offset) each other.

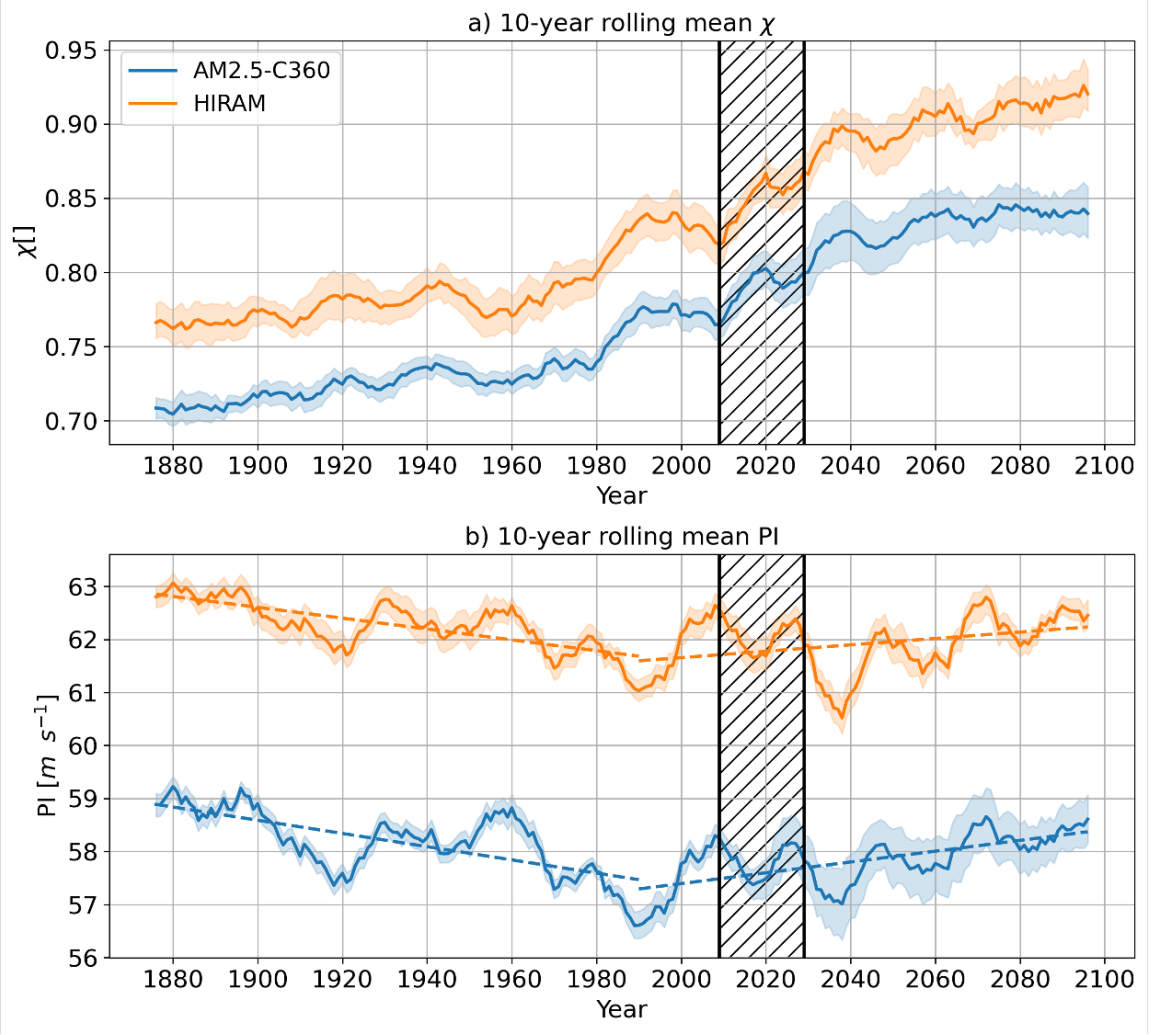

591 FIG. 7. Similar to Figure 5, but for the thermodynamic variables: (a) χ and (b) PI. Dotted trend lines are fitted
592 for PI over the distinct periods with opposite trends (1871-1990 with a decreasing trend and 1990-2100 with an
593 increasing trend) in both models.

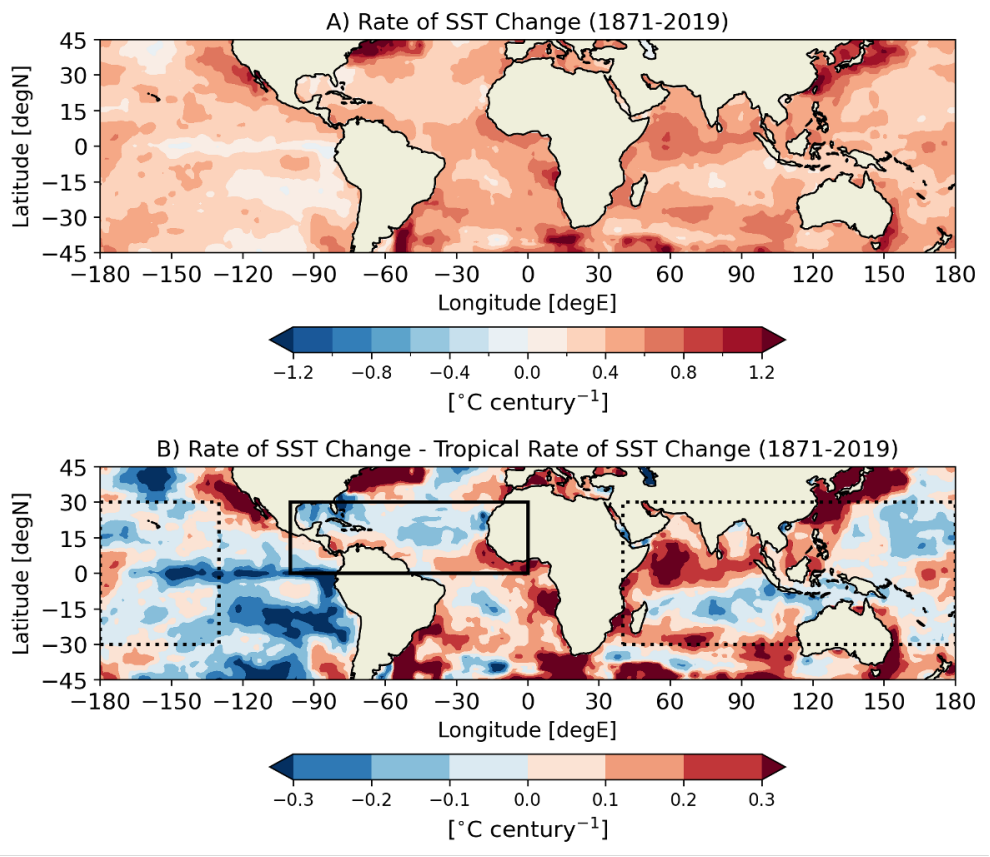

FIG. 8. (a) The rate of historical observed TC season SST changes from 1871 to 2019, with SSTs sourced from Chan et al. (2021). (b) The difference between (a) and the mean tropical TC season SST change rate over the same period. In (b), the solid black box highlights the tropical Atlantic basin, while the dotted black box marks the Indo-Pacific Warm Pool region, as defined by Weller et al. (2016), which typically encompasses the warmest ocean surface waters on Earth.

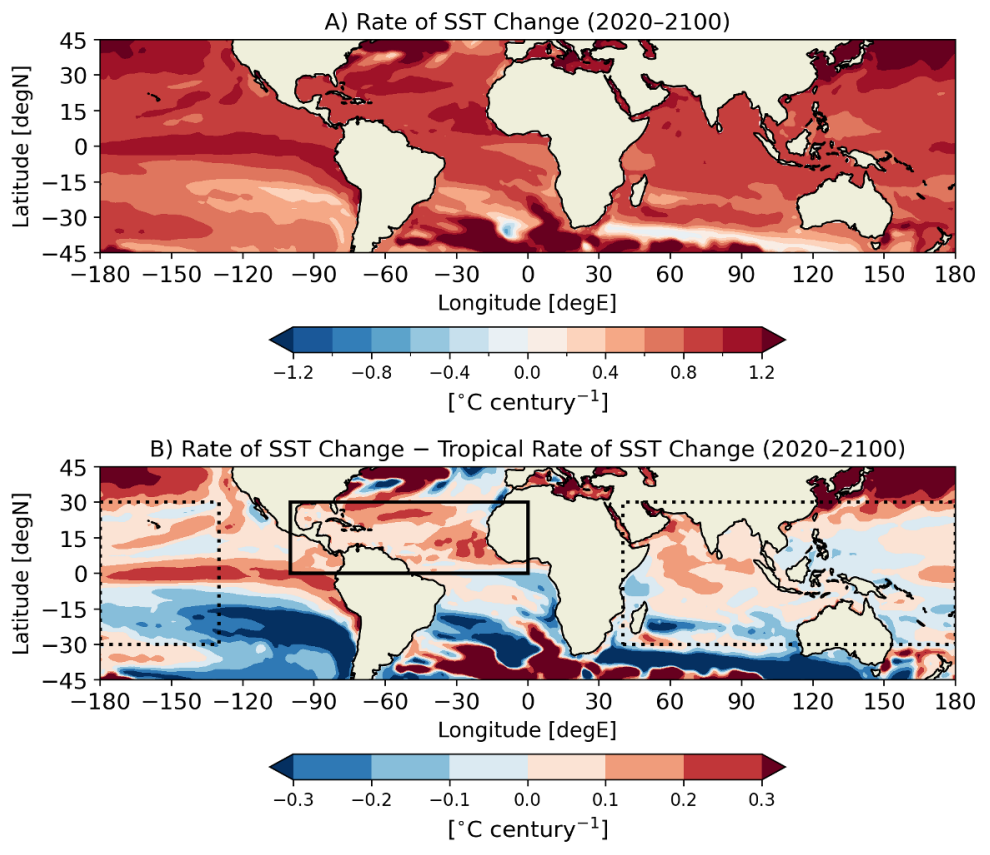

FIG. 9. Same as Fig. 8, but for the future projected period 2020–2100. Both panels show projected SSTs used to force the *rcp45 flor* experiment, detailed in Section 2.

(ii) Dynamic variables

While the relationship between thermodynamic variables is a primary driver of the potential trend (or lack thereof) in $P(\Lambda)$, we also examine the role of the ventilation index (Eq. 11), specifically vertical wind shear, as a potential contributor to changes in $P(\Lambda)$. Figure 10b presents the time series of vertical wind shear across both models throughout the entire record. Both models simulate similar magnitudes of wind shear in the historical and projected periods. During the historical period, especially from 1950 to 2000, wind shear increases, making conditions progressively less favorable for storm activity. In contrast, the projected period shows no clear trend in wind shear: in AM2.5-C360, wind shear remains relatively stable, whereas in HIRAM, it exhibits multidecadal and decadal variability. In HIRAM's projected period, wind shear is elevated between approximately

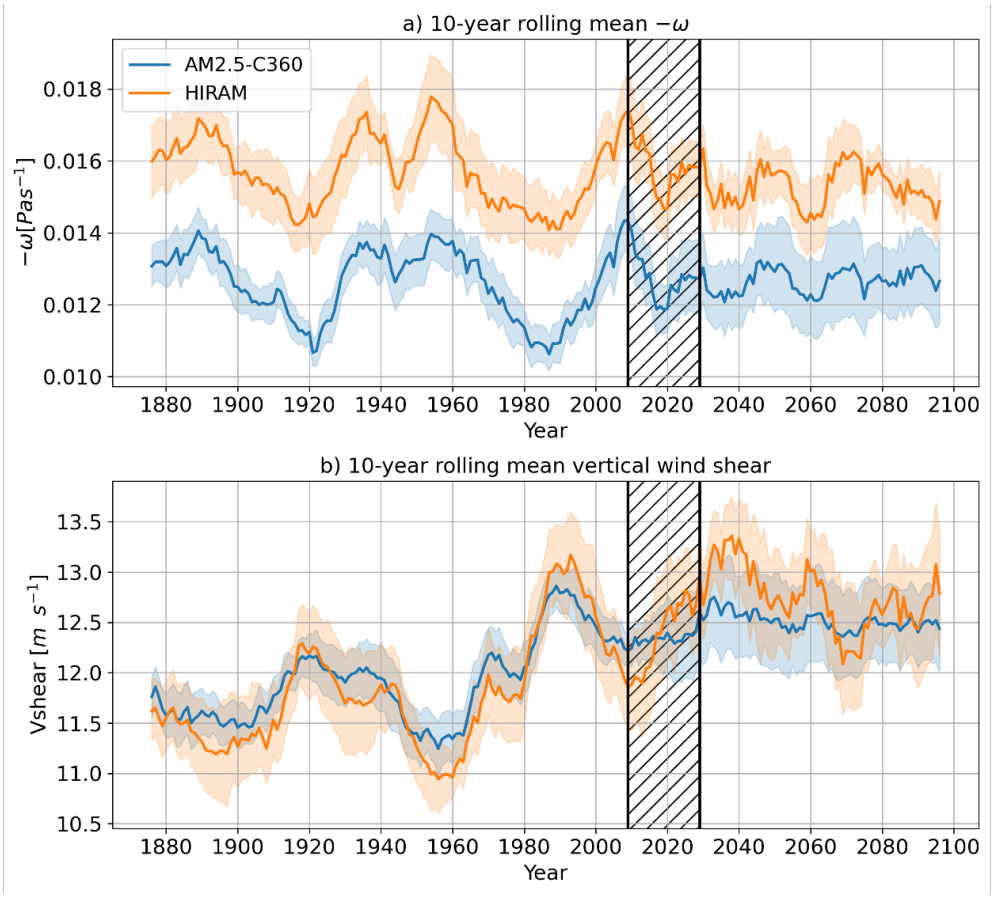

FIG. 10. Similar to Fig. 7, but for the dynamic variables: (a) $-\omega$ and (b) vertical wind shear.

2020 and 2070 and is characterized by decadal-scale fluctuations, with relative maxima around 2050, 2060, and 2080 and minima near 2050 and 2070.

The increasing wind shear during the historical period, especially during the 1960-1990 period, likely amplified the already declining TC favorability, as both thermodynamic and dynamic conditions became less conducive to storm development. In the projected period, however, where thermodynamic variables counterbalance each other, wind shear has the potential to influence the overall trend in $P(\Lambda)$. Yet, since wind shear remains largely steady, $P(\Lambda)$ also remains unchanged in the projected period.

To investigate the physical mechanisms underlying changes in vertical wind shear in the tropical Atlantic TC basin, particularly the increase during 1960–1990 and the relative stability in the future projections, we examine ensemble-mean, zonally averaged atmospheric temperature changes in both models (Figure 11). Because our analysis focuses on seasonal and ensemble means over

the broad tropical Atlantic region (10°N–30°N), we assume the large-scale flow is in approximate geostrophic balance. Under this assumption, the thermal-wind relationship provides a useful approximation for the zonal component of vertical wind shear in terms of the meridional temperature gradient. We approximate the zonal component of the vertical wind shear between 850 hPa and 250 hPa using the thermal-wind balance:

$$u(250) - u(850) = -\frac{R}{f} \ln\left(\frac{850}{250}\right) \frac{\partial \overline{T}}{\partial y}, \tag{13}$$

where $u(250) - u(850)$ represents the approximated zonal wind shear between 250 hPa and 850 hPa, R is the gas constant for dry air, f is the Coriolis parameter, and $\partial \overline{T}/\partial y$ is the meridional gradient of the layer-mean temperature.

The layer-mean temperature $\overline{T}$ is defined as the log-pressure–weighted mean temperature between 850 hPa and 250 hPa:

$$\overline{T} = \frac{1}{\ln\left(\frac{850}{250}\right)} \int_{250}^{850} T(p)\, d\ln p, \tag{14}$$

where $T(p)$ denotes temperature at pressure level p. This definition is equivalent to the temperature that governs the thickness of the 850–250 hPa layer and therefore directly controls the vertical wind shear through the thermal-wind relationship. We compute this shear proxy using ensemble-mean, seasonally averaged, and zonally averaged temperature profiles from each model during both the historical and future projection periods. The meridional temperature gradient is then evaluated and averaged over 10°N–30°N using cosine-latitude weighting. Both models resolve 11 atmospheric pressure levels between 850 hPa and 250 hPa, allowing for a robust calculation of the log-pressure–weighted mean temperature. The resulting time series of the ensemble-mean thermal-wind shear proxy for both models is shown in Figure 11.

First, we note that the magnitude of the thermal-wind shear proxy differs by approximately an order of magnitude from the explicitly simulated vertical wind shear shown in Figure 10, and that the proxy magnitudes also differ between the two models. In AM2.5-C360, the proxy shear ranges from approximately 3–4 m s^{-1}, while in HIRAM it ranges from roughly 5–7 m s^{-1}. In contrast, the vertically resolved wind shear simulated directly by both models ranges from approximately 11–13 m s^{-1}.

Despite these differences in magnitude, the temporal evolution of the shear proxy closely tracks that of the explicitly simulated vertical wind shear. Both the proxy and the simulated shear exhibit predominantly multidecadal variability during the historical period, including a pronounced peak between 1910 and 1950 and a marked increase during 1960–1990, features that are evident in both models. The projected evolution of the shear proxy similarly mirrors that of the explicitly simulated shear. In HIRAM, both records display a clear multidecadal maximum from 2020–2050, followed by decadal-scale peaks during 2050–2070 and 2070–2090. In contrast, the AM2.5-C360 future projections show relatively stable wind shear in both the proxy and the explicitly simulated fields, with little evidence of pronounced decadal or multidecadal variability. Together, these results suggest that changes in the spatial structure of meridional temperature gradients largely govern the decadal and multidecadal evolution of vertical wind shear in both models. More broadly, they reinforce the conclusion that spatial patterns of temperature change, rather than basin-wide mean warming alone, play a central role in modulating environmental conditions, such as vertical wind shear, that influence TC development.

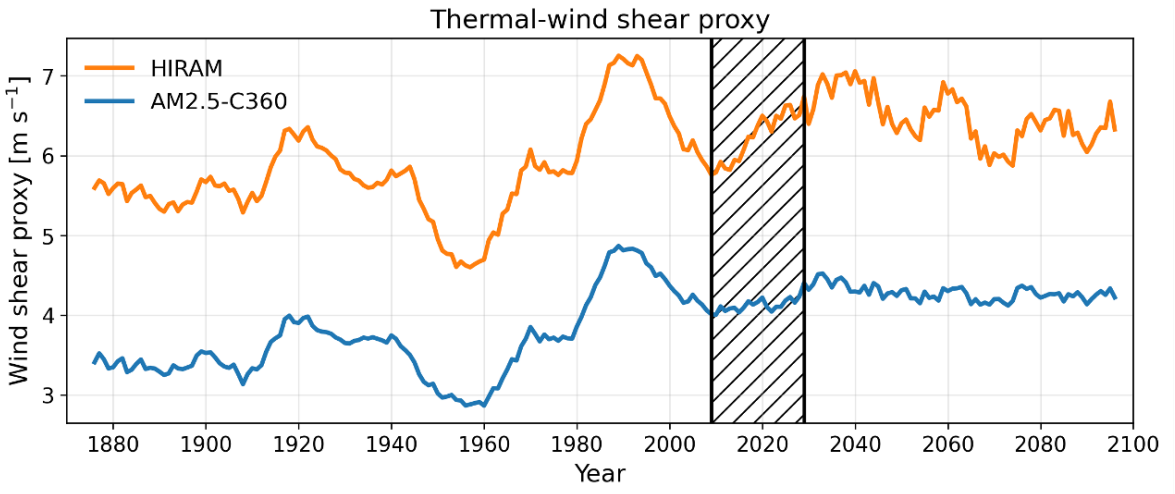

FIG. 11. Ten-year rolling mean time series of the thermal-wind shear proxy defined in Eq. 13 for AM2.5-C360 (blue) and HIRAM (orange). Lines show the ensemble-mean zonal shear between 250 and 850 hPa averaged over 10°–30°N. The historical segment (1871–2019) is derived from the *obs sst* simulations, while the future segment (2020–2100) is derived from the *rcp4.5 sst* simulations. The two periods are concatenated to form a continuous time series. Values to the left of the hatched region correspond to simulations forced with observed SSTs (*obs sst*), while values to the right correspond to simulations forced with observed climatology plus projected SST patterns (*rcp45 flor*). The hatched region marks a smooth transition that blends both forcing regimes.

Next, because changes in SPI are primarily driven by variations in $-\omega$, we analyze the temporal evolution of this variable in Figure 10a. Just as SPI exhibits no clear trend across the full record in either model (Fig. 5b), $-\omega$ similarly shows no discernible long-term trend. However, both variables display pronounced multidecadal variability in the historical period, with a maxima from 1930-1970 and minima from 1900-1930 and 1960-2010. In the future projections, we observe decadal-scale peaks and troughs. Additionally, while the typical magnitude of $-\omega$ is greater in HIRAM than in AM2.5-C360, both models exhibit comparable temporal variability. As detailed in Appendix Section c, since vorticity does not play an important role in driving TC changes, we do not include a discussion of this dynamic variable here.

4. Discussion and conclusions

As shown in Figure 4, the TC framework described in Hsieh et al. (2020) ($SPI \times P(\Lambda)$) successfully reproduces Atlantic TC variability in simulations forced with observed SSTs, as well as in projections under an RCP4.5 SST increase. Its performance is slightly stronger in HIRAM than in AM2.5-C360, particularly during projected period, during which the theoretical framework in AM2.5-C360 tends to underestimate the projected TCs (Figures 3 and 4). Importantly, the framework achieves this skill without calibration or tuning, underscoring its ability to capture TC variability directly from local large-scale environmental conditions. This is particularly noteworthy in the Atlantic basin, where TCs frequently originate from nonlocal disturbances such as African easterly waves (AEWs; Emanuel (2022)). In contrast to other widely used TC proxies such as genesis potential indices (GPIs), the framework presented by Hsieh et al. (2020) explicitly incorporates the initial seed disturbances associated with AEWs that initiate TC formation (Cavicchia et al. 2023). Most GPIs require calibration prior to application in future climate scenarios (Camargo et al. 2014) and exhibit limited skill in reproducing interannual and multidecadal TC variability (Cavicchia et al. 2023). Together, these findings highlight the robustness of the $SPI \times P(\Lambda)$ framework for assessing Atlantic TC variability across both historical and projected climates.

Using the theoretical framework and explicitly tracked TCs from a suite of idealized simulations in both AM2.5-C360 and HIRAM, we assess the relative roles of regional SST pattern changes and global mean warming in modulating Atlantic TC activity during both the historical and projected periods. During the historical period, we compare an experiment that includes both global mean

and patterned warming (*obs sst*) with an experiment that isolates patterned warming and removes the global mean signal (*rm warming*). We find that both the tracked TC counts and the framework-derived TC variability are indistinguishable between these experiments, indicating that global mean warming played a minimal role in historical Atlantic TC variability. Instead, regional SST patterns dominated past variations in storm activity.

In the future projected period, we evaluate TC sensitivity to global mean warming by contrasting an experiment that includes both patterned and mean warming (*rcp45 flor*) with experiments that include only uniform global mean warming (*cntl* and *2K 2CO2*). Across both models and TC representations (explicit tracking and the theoretical framework), we identify statistically significant differences in TC sensitivity to mean warming between experiments that do and do not include patterned warming. In HIRAM, in particular, the sign of the TC trend differs between experiments: when both patterned and mean warming are present, TC counts exhibit no statistically significant trend, whereas under uniform mean warming alone, TC counts decline. Together, these results underscore the critical role of regional warming patterns in shaping Atlantic TC activity. Assessments of future TC changes cannot rely solely on global mean warming trends; accounting for spatial patterns of warming is essential for drawing robust statistical conclusions about TC sensitivity to climate change.

Our results emphasizing the importance of regional SST warming patterns in driving changes in Atlantic TC activity are consistent with the findings of Vecchi et al. (2019), Villarini et al. (2011b), Knutson et al. (2015), Vecchi and Soden (2007). These studies further suggest that SST spatial patterns do not exert a first-order influence on TC responses to warming in other ocean basins. They argue that this distinction arises because relative SST anomalies in the North Atlantic under transient $2\times CO_2$forcing in AM2.5-C360 and HIRAM are substantially larger than those in other TC basins. We find similar behavior in the future SST projections used in the *rcp45 flor* experiment, which are derived from the FLOR RCP4.5 model. As shown in Figure 13, the projected rate of relative SST change in the Atlantic main development region is markedly larger (+0.25 °C per century) than in other basins, including the western Pacific (-0.05 °C per century) and the Indian Ocean (+0.10 °C per century). Together, these results support the conclusion that regional warming patterns play a particularly critical role in shaping TC variability in the Atlantic, with a weaker influence in other ocean basins where relative SST contrasts are smaller. This pattern

likely includes a radiatively-forced component, but there are currently large disagreements about the sign and magnitude of such forcing (e.g. Zhuo et al. (2025)).

Next, we analyze how the large-scale dynamic and thermodynamic variables contribute to changes in parameterized TCs during both the historical and projected periods. Examining the temporal evolution of SPI (Fig. 5b), we find no clear long-term trend. Instead, SPI is governed by multidecadal and decadal fluctuations, largely modulated by variability in $-\omega$. In contrast, the temporal evolution of $P(\Lambda)$ is characterized by a distinct decreasing trend during the historical period, followed by a relatively stable plateau in the projected period (Fig. 5a). Notably, from 2020-2100 $P(\Lambda)$ exhibits little decadal variability, particularly in AM2.5-C360. The difference in $P(\Lambda)$'s variability between both record periods is primarily driven by the relationship between its thermodynamic components: moist entropy deficit (χ) and potential intensity (PI). During the historical period, particularly from 1871-1990, PI and χ had a compounding effect, both becoming increasingly unfavorable for TC activity and reinforcing the decline in $P(\Lambda)$. However, in the future projection with FLOR SSTs, their opposing influences cancel out, leading to a stable $P(\Lambda)$ with no clear trend.

This shift in the thermodynamic relationship is evident in spatial analyses, where we observe a statistically significant increasing trend in Λ during the historical period (Fig. 12), thus becoming less favorable for TCs, whereas no such trend is apparent in the projected period (Fig. 13). This highlights how the changing interaction between PI and χ fundamentally alters the behavior of Λ, $P(\Lambda)$, and parametrized TCs, over time.

The reversal in the relationship between χ and PI across the historical and projected periods arises from a shift in PI trends (Figure 7). While χ increases steadily throughout both periods, PI declines during the historical interval from 1871 to 1990 and increases thereafter. In the projected period, both PI and moisture deficit increase, consistent with prior studies that project rising global PI and moisture deficit through the late 21st century (e.g., Emanuel et al. (2008), Emanuel (2021b), Lee et al. (2020)).

Our historical results also show a pronounced increase in PI from 1990 to 2020 (Figure 7), in agreement with Kossin and Camargo (2009) and Emanuel (2021a), who analyze PI evolution using reanalysis products and likewise identify a sharp post-1980/1990 increase. The NCEP/NCAR reanalysis used in Kossin and Camargo (2009) spans 1948–2008 and therefore captures only the

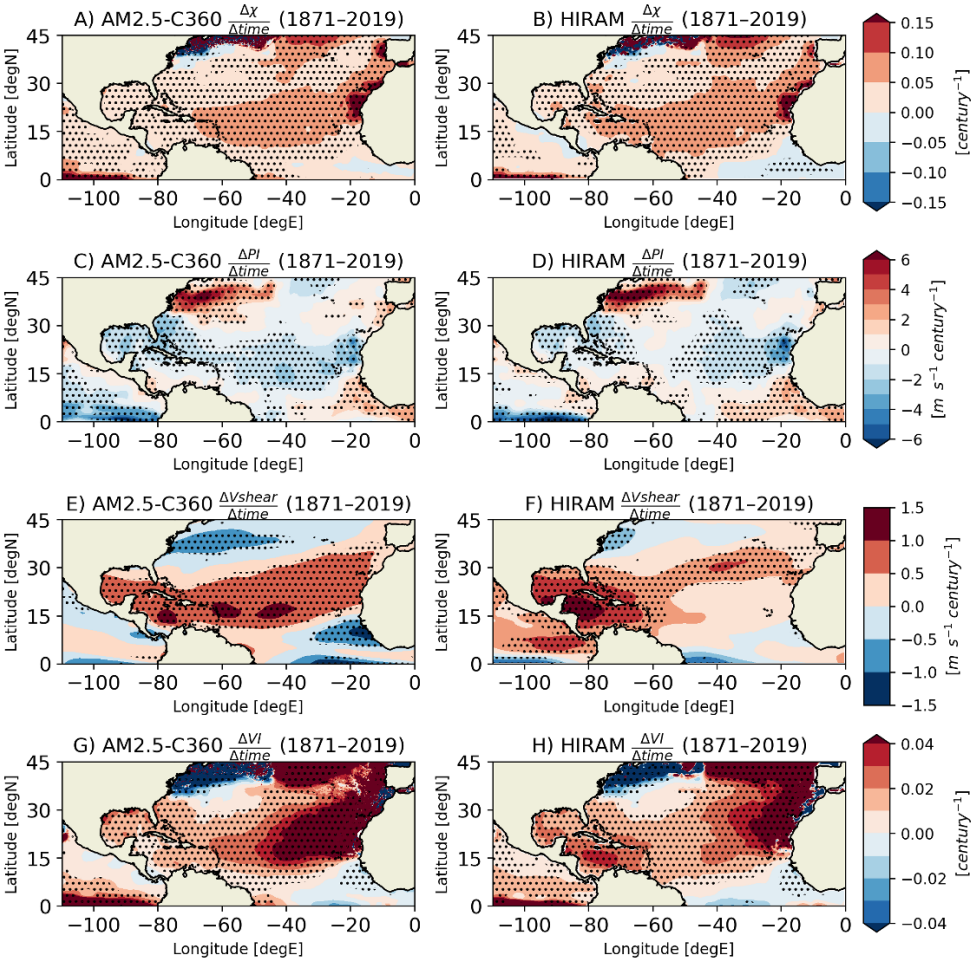

771 FIG. 12. Linear regression coefficients for the century-scale TC-season rate of change in (a, b) χ, (c, d) PI, (e,
772 f) vertical wind shear, and (g,h) ventilation index (Λ) during the historical period (1871–2019) for AM2.5-C360
773 and HIRAM. Dotted regions indicate statistically significant trends ($p < 0.05$).

784 latter portion of our multi-century record; nevertheless, both studies exhibit decreasing PI from
785 roughly 1950 to 1990 followed by an increase thereafter. Emanuel (2021a), using the ECMWF
786 CERA-20C reanalysis (Laloyaux et al. 2018) covering 1901–2010, find multidecadal PI variability
787 from 1901 to 1980 without a clear long-term trend, with a peak near 1950 and troughs around 1920
788 and 1970. Our results similarly show decadal PI variability over this period, with troughs near 1920
789 and 1970, but with a peak closer to 1960 and an overall declining trend from 1901 to 1980. While
790 both studies agree on the timing of PI minima and the rapid increase after 1980-1990, differences

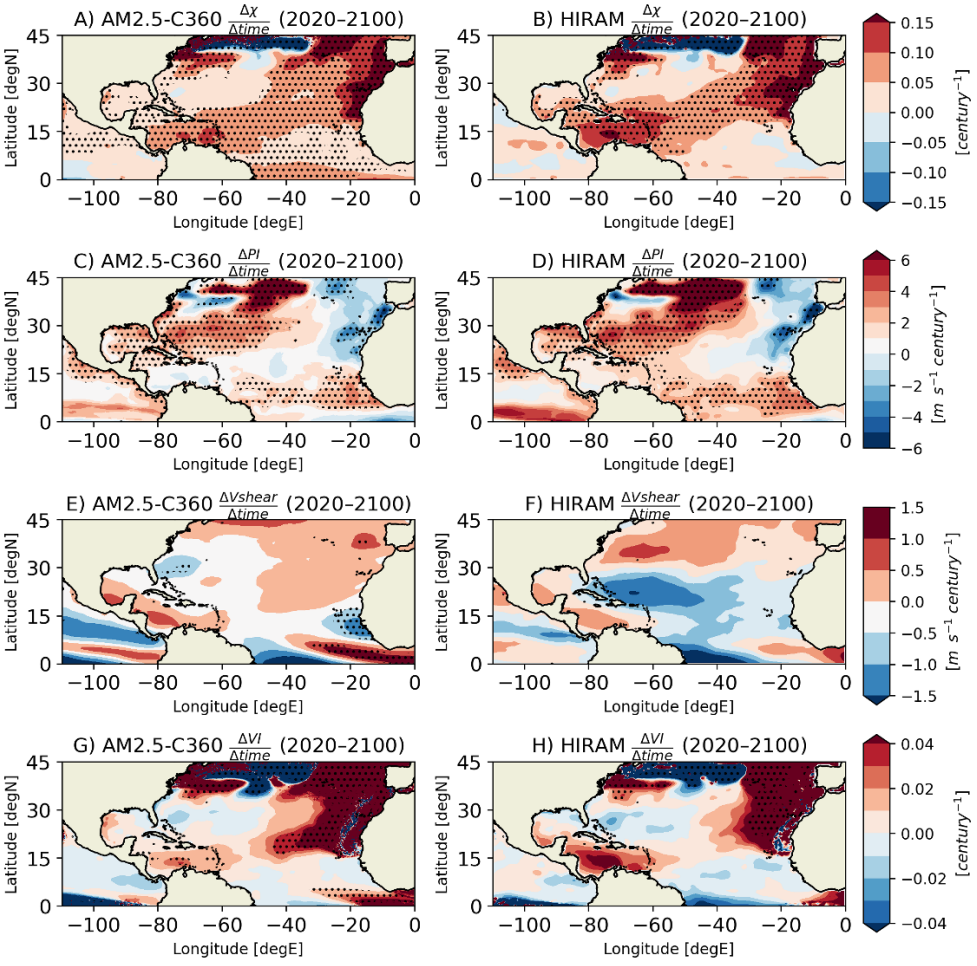

FIG. 13. Same as Fig. 12 but for the projected period (2020-2100).

in peak timing and long-term trend prior to 1980 likely reflect biases in reanalysis products during the pre-satellite era.

We attribute the reversal in PI trends between the historical and projected periods to differences in the relative warming rates of the tropical Atlantic and the broader tropics, which are known to be important in modulating TC activity (Vecchi and Soden (2007); Villarini et al. (2010)). During the historical period, the tropical Atlantic warmed more slowly than the rest of the tropics, likely weakening the temperature contrast between the sea surface and the upper troposphere. Conversely, in the projected period, Atlantic SSTs are expected warm faster than the rest of the tropics, enhancing the surface-to-upper troposphere temperature contrast and fostering conditions

more favorable for increases in PI and TC activity. This underscores the critical role of regional SST patterns, rather than just mean warming trends, in shaping Atlantic TC activity.

These findings highlight the deep uncertainty in future TC projections (Knutson et al. 2020), a challenge that dates back to the earliest model-based study of TC frequency (Broccoli and Manabe 1990). The strong compensation between thermodynamic variables, consistent with results from downscaled CMIP6 simulations (Emanuel 2021b), suggests that these variables, directly influenced by warming, are unlikely to be the primary drivers of TC activity changes. Instead, dynamic variables such as vertical wind shear, which are indirectly linked to warming through circulation changes, emerge as key determinants of future TC trends. However, because these dynamic variables are not directly constrained by warming, their future behavior remains highly uncertain (Pfahl et al. 2017).

Regional temperature patterns play a fundamental role in shaping both thermodynamic and dynamic variables, including wind shear and $-\omega$, through thermal wind balance and by setting the most active convective regions. Stronger meridional temperature gradients enhance vertical wind shear, while high relative SST patterns intensify deep tropical convection. Ultimately, regional SST patterns and the processes that control the vertical structure of warming may greatly influence changes in the dynamic variables, reinforcing the importance of spatial temperature distributions in determining future TC activity.

Building on our argument that the compensation of thermodynamic variables enables dynamic factors to influence TC activity, we observe that the trend in $P(\Lambda)$ closely mirrors that of vertical wind shear in model simulations, which is primarily determined by temperature patterns. As shown in Figure 11, vertical wind shear increases during the historical period, driven by a strengthened atmospheric meridional temperature gradient. However, these trends do not persist in future projections (Figure 13e), and substantial inter-model differences arise. For example, AM2.5-C360 forecasts a reduction in shear along the U.S. East Coast, whereas HIRAM predicts an increase in the same region. Since neither model shows a consistent basin-wide trend in shear, the projected trend in $P(\Lambda)$ remains similarly uncertain. This ambiguity in shear trends is likely due to differences in projected atmospheric temperature.

The dominant role of thermodynamic variable compensation in regulating $P(\Lambda)$ reinforces the idea that, given the uncertainty in $P(\Lambda)$ projections, future TC activity will be primarily modulated

by changes in SPI, which represents the number of basin-wide seeds. This aligns with previous studies such as Hsieh et al. (2020), Vecchi et al. (2019), Sugi et al. (2020), and Yamada et al. (2021), which emphasize the critical role of TC seeds in shaping future TC activity. Our findings support this conclusion, as the projected stability of $P(\Lambda)$ (Fig. 5a) suggests that the decadal variability of parametrized TCs ($SPI \times P(\Lambda)$; Fig. 4) largely follows the variability of SPI (Fig. 5) and $-\omega$ (Fig. 10a).

While some previous studies suggest that the global number of TC seeds may decrease in a warmer climate (Hsieh et al. (2020), Vecchi et al. (2019), Sugi et al. (2020), Yamada et al. (2021)), our findings indicate that SPI, our seed proxy, does not exhibit a clear Atlantic basin-wide trend in either the historical or projected periods. Instead, Atlantic SPI is characterized by decadal and multidecadal variability driven by fluctuations in $-\omega$. Although no basin-wide trends in $-\omega$ emerge, we identify localized trends within the basin, particularly along the ITCZ and within the TC main development region (Fig. 14). Specifically, an eastward shift in $-\omega$ is evident in the deep tropics, with a decreasing trend in the western basin and an increasing trend in the eastern basin, which could be as result higher rate of warming in the eastern tropical Atlantic than the western tropical Atlantic (Fig. 9b). This pattern suggests a potential eastward shift in TC genesis under warming conditions (Kortum et al. (2024)), and mirrors some observed eastward shifts in Atlantic TC tracks (Colbert and Soden 2012; Vecchi and Knutson 2011). However, significant uncertainties remain in $-\omega$, as vertical velocity and seed development could be influenced by radiative feedbacks linked to cloud processes or unresolved mechanisms, as described in the gross moist stability framework (Hsieh et al. (2023), Neelin and Held (1987)).

It is important to recognize the inter-model differences present in our results, such as variations in the framework's ability to capture TC activity in idealized simulations and discrepancies in future projections of vertical wind shear, which we suggest have to do with differences in the pattern of warming and TC seed distribution. This study examines only two atmosphere-only models, both of which have been shown to predict the highest number of future TCs compared to other model simulations (Bhatia et al. (2018), Hsieh et al. (2022)). However, as noted by Knutson et al. (2020), most dynamical TC-resolving models project a decrease in storm activity in a warming climate. Furthermore, because the models used here are atmosphere-only and forced exclusively by SSTs, they may highlight the limitations of relying on SSTs alone for TC predictions, an issue

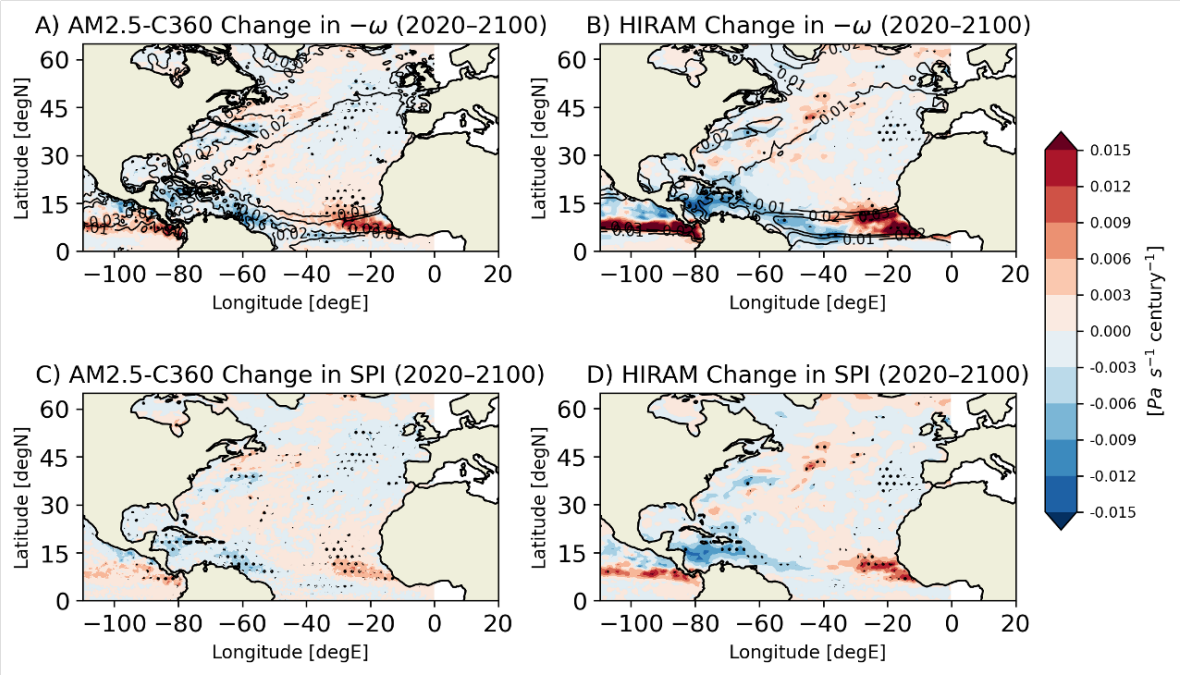

Fig. 14. Linear regression coefficients for the century-scale TC-season rate of change in (a, b) $-\omega$ and (c, d) SPI during the projected period (2020–2100) for AM2.5-C360 and HIRAM. Dotted regions indicate statistically significant trends ($p < 0.05$). In (a) and (b), black contours show the mean TC-season $-\omega$ during the historical period (1871–2019). Red (blue) shading represents regions with increasing ascent (descent) in the projection period.

that became particularly evident during the 2020 TC season (Fig. 1). As suggested by Kortum et al. (2024), factors such as atmospheric chaos, aerosols, and other environmental influences could play a critical role in modulating TC activity, potentially introducing biases in SST-forced models.

Beyond the aforementioned caveats, our results highlight that regional SST and atmospheric temperature patterns, rather than the global-mean warming trend alone, play a central role in shaping both historical and future Atlantic tropical cyclone (TC) activity. In particular, the relationship between PI and χ is strongly modulated by the relative rate of warming in the tropical Atlantic compared to the broader tropics. Likewise, the behavior of key dynamical variables is governed by spatial temperature gradients rather than uniform warming.

Substantial uncertainties remain in projections of future SST patterns, especially in the Atlantic and other tropical basins such as the eastern Pacific (Seager et al. (2022); Shaw et al. (2024)). In

the Atlantic, for example, the magnitude of future Atlantic Meridional Overturning Circulation (AMOC) weakening is poorly constrained, with potentially important implications for regional SST evolution (Cheng et al. (2013); Srokosz and Bryden (2015)). More broadly, most climate models project a shift toward an El Niño–like mean state, characterized by enhanced warming in the eastern Pacific, whereas observations suggest a tendency toward a La Niña–like state with comparatively weaker eastern Pacific warming (Zhuo et al. 2025). Consistent with the multi-model mean, our simulations exhibit an El Niño–like shift (Figure 13), with eastern Pacific SSTs warming more rapidly than the rest of the basin.

Changes in the mean state of the tropical Pacific may influence Atlantic TC seed formation; for example, Hsieh et al. (2022) show that La Niña conditions are more favorable for Atlantic SPI. However, the impact of Pacific SST changes on PI is likely more muted. This is because the warmest tropical SSTs, typically associated with the western Pacific warm pool, largely set upper-tropospheric temperatures across the tropics through convective adjustment, thereby exerting a dominant control on PI. Consistent with this mechanism, Eusebi et al. (2025) demonstrate that the relative difference between tropical Atlantic SSTs and the warmest tropical SSTs, rather than the tropical-mean SST, provides a more robust predictor of Atlantic TC PI. Together, these results underscore the importance of accurately representing regional temperature patterns across the global tropics, as their influence on Atlantic TCs can arise through distinct physical pathways. Improving the reliability of future TC projections therefore requires tighter constraints on projected SST pattern changes across a diverse ensemble of climate models.

Acknowledgments. We thank Gabriele Villarini, Stephan Fueglistaler, Andrew Williams, Nadir Jeevanjee, and Hiroyuki Murakami for discussion and comments. This work has been supported in part by a grant from the Heising-Simons foundation and the Carbon Mitigation Initiative at Princeton University, funded by BP. E.L. was supported by the National Science Foundation Graduate Research Fellowship. The simulations were performed on computational resources managed and supported by Princeton Research Computing, a consortium of groups including the Princeton Institute for Computational Science and Engineering, the Office of Information Technology's High Performance Computing Center, and the Visualization Laboratory at Princeton University.

Data availability statement. Source code of the HiRAM model is available from `https://www.gfdl.noaa.gov/hiram-quickstart`. ERA5 data are available from `https://cds.climate.copernicus.eu/datasets/reanalysis-era5-pressure-levels-monthly-means?tab=overview`, and MERRA2 data are available from `https://gmao.gsfc.nasa.gov/gmao-products/merra-2/data-access_merra-2/`.

APPENDIX

Further evaluation of the seed-probability framework and its components

a. Verifying SPI Theory

To assess whether the SPI framework can faithfully reproduce the climatology and variability of tracked TC seeds in both models, we compare the spatial distribution of tracked seeds and SPI during the historical period (Figure A1) and examine time series of tracked seeds and SPI for both the historical and projected periods (Figure A2). We first examine the spatial climatology of tracked seeds and SPI during the historical period. HIRAM exhibits a stronger sensitivity to seed formation than AM2.5-C360: the climatological mean seed density in AM2.5-C360 ranges from approximately 20–60 seed days per year per $10^\circ \times 10^\circ$ grid box, whereas in HIRAM it ranges from roughly 5–15 seed days per year per $10^\circ \times 10^\circ$ grid box. As described in Section 2, the same seed-tracking algorithm is applied to both models. Consequently, these differences arise from distinct realizations of the atmospheric vorticity field, which is the key dynamical component of the seed-tracking framework. Consistent with the seed climatology, the climatological mean SPI

also exhibits stronger sensitivity in HIRAM than in AM2.5-C360, with typical SPI values in active regions of 0.0075–0.0125 Pa s^{-1} in HIRAM compared to 0.010–0.015 Pa s^{-1} in AM2.5-C360.

Importantly, the SPI framework successfully reproduces the primary spatial features of seed formation in the tropical Atlantic. In both models, SPI captures two prominent maxima: one in the main development region near the West African coast between approximately 5°–15°N, and a second in the central Atlantic between 25°–30°N. The framework also correctly identifies regions of suppressed seed formation, including north of Colombia and Venezuela, south of Cuba, and in the western Gulf of Mexico. In addition, SPI reproduces a pronounced minimum in seed activity off the west coast of subtropical Africa between 15°–30°N. Together, these results demonstrate that the SPI framework faithfully captures the observed spatial distribution of TC seeds in both models.

We next examine normalized time series of historical and future projected SPI and tracked seed counts. In both models, SPI closely reproduces the decadal and multidecadal variability in seed formation. Specifically, the framework captures the multidecadal peak in seed activity from approximately 1920–1980, including an enhanced decadal maximum during 1950–1960. SPI also reproduces several decadal peaks throughout both the historical and projected periods, including a pronounced increase from 2000–2020 in both models. The strong correlation between ensemble-mean SPI and tracked seed counts ($r = 0.86$ in AM2.5-C360 and $r = 0.73$ in HIRAM) further demonstrates the ability of the SPI framework to capture variability in seed formation across the extended record. Overall, the results shown in Figures A1 and A2 indicate that the SPI theory provides a robust representation of TC seed formation in both models. This gives us confidence in applying the full theoretical framework, $SPI \times P(\Lambda)$, to approximate TC counts.

b. Covariance between seed and probability proxies

We assess the correlation coefficient between the annual TC-season basin-averaged SPI and $P(\Lambda)$ (Fig. A3) for both the observed historical period (1871-2019) and the projected future period (2020-2100). Our analysis reveals that, across both models and time periods, the ensemble mean of SPI and $P(\Lambda)$ exhibit a moderate correlation. Specifically, for each model, the ensemble mean correlation between the proxies is consistent across the observed and projected periods ($r \sim 0.5$ for AM2.5-C360 and $r \sim 0.7$ for HIRAM), with HIRAM generally showing stronger correlations. In AM2.5-C360, the correlation varies more widely across ensemble members, ranging from $r = 0.25$

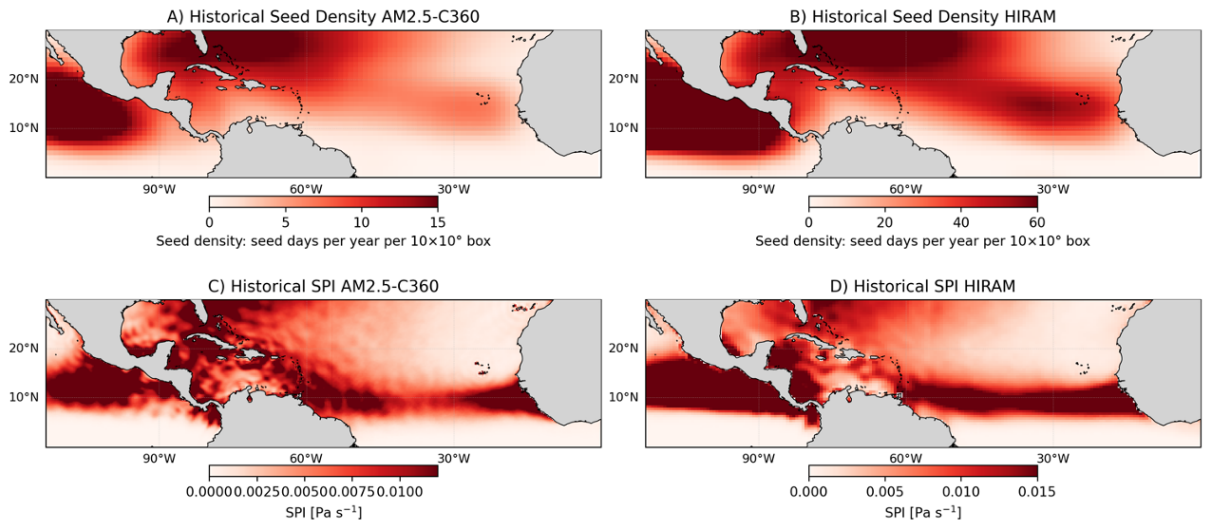

FIG. A1. Mean spatial density of Atlantic tropical cyclone seed locations during the historical period (1871–2019) in (a) AM2.5-C360 and (b) HIRAM. Density is defined as the annual mean number of seed days within each model grid cell, aggregated onto 10° × 10° latitude–longitude bins. Panels (c) and (d) show the mean seasonally averaged (June–November) seed probability index (SPI) during the historical period for AM2.5-C360 and HIRAM, respectively.

to $r = 0.55$, while in HIRAM, the spread is narrower, with correlations ranging from $r = 0.5$ to $r = 0.7$. Despite the variation in ensemble spread and inter-model differences, it is evident that SPI and $P(\Lambda)$ are not independent, but rather covary in a manner that reflects a spatio-temporal relationship, with their combined behavior serving as a proxy for TC activity.

c. Vorticity

To show that changes in the vorticity term of the SPI have a negligible impact on variations in TC activity, we perform a logarithmic decomposition of the SPI, allowing the terms to be expressed additively:

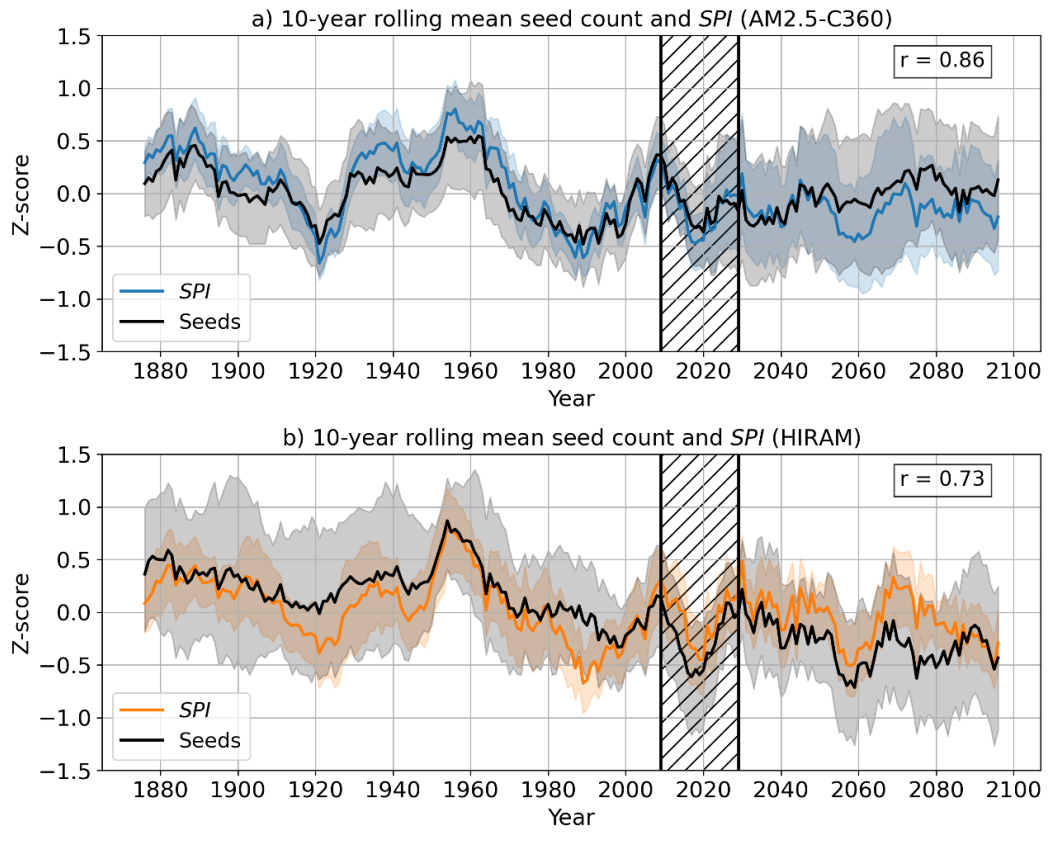

950 FIG. A2. Normalized 10-year rolling mean of simulated Atlantic TC seed frequency (black) and parameterized
951 seed frequency (SPI; colored) for (a) AM2.5-C350 (blue) and (b) HIRAM (orange). Shaded regions indicate
952 the bootstrapped 95% confidence intervals as in Fig. 4. The historical period (1871–2019) is based on the
953 obs SST simulation, whereas the future period (2020–2100) is derived from the rcp4.5 SST simulation. These
954 two periods are combined into a continuous time series, with both simulated and parameterized TC frequencies
955 standardized using a Z-score normalization, as in Fig. 4. Correlation coefficients between the ensemble mean
956 simulated and parameterized TC frequencies are displayed in the top right corner of each panel. Values to the
957 left of the hatched region correspond to simulations forced with observed SSTs (*obs sst*), while values to the
958 right correspond to simulations forced with observed climatology plus projected SST patterns (*rcp45 flor*). The
959 hatched region marks a smooth transition that blends both forcing regimes.

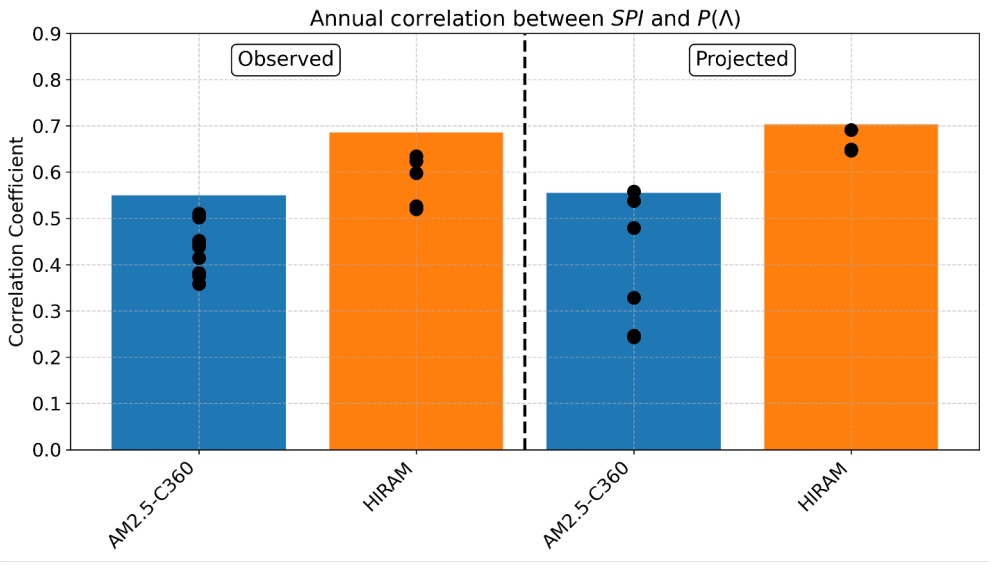

FIG. A3. Annual TC-season basin mean correlation coefficient between SPI and $P(\Lambda)$ in AM2.5-C360 (blue) and HIRAM (orange) in the *obs SST* simulation (left) and *rcp4.5 SST* simulation (right). Bars indicate the ensemble mean correlation, while black dots represent individual ensemble members.

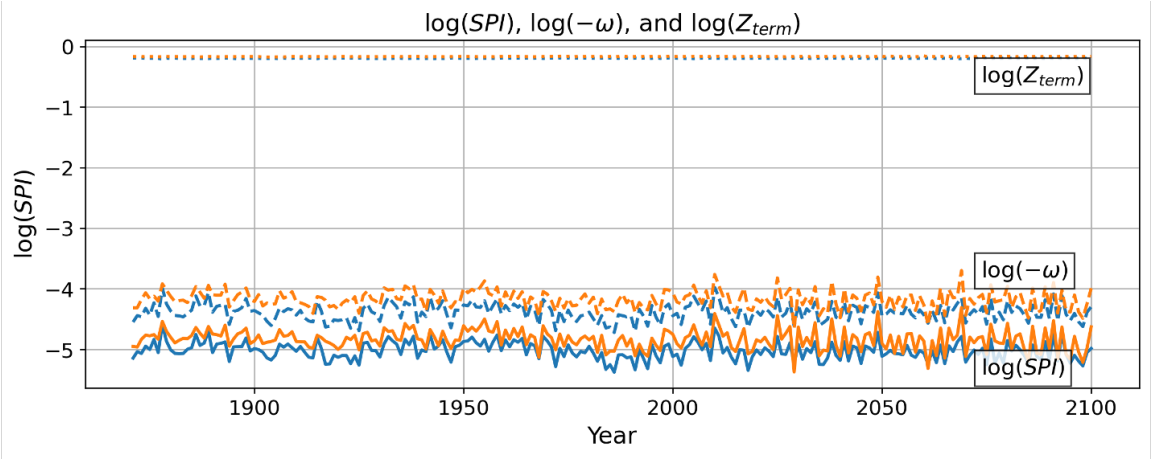

FIG. A4. Annual ensemble mean seasonally and basin-averaged $\log(SPI)$ (solid lines), $\log(-\omega)$ (dashed lines), and $\log(Z_{term})$ (dotted lines) in AM2.5-C350 (blue) and HIRAM (orange). The historical period (1871–2019) is based on the *obs SST* simulation , whereas the future period (2020–2100) is derived from the *rcp4.5 SST* simulation. These two periods are combined into a continuous time series.

$$
\begin{aligned}
SPI &= \underbrace{-\omega}_{\text{vertical velocity}} \times \underbrace{\frac{1}{1+Z^{-1/0.69}}}_{\text{vorticity term } (Z_{term})} \\
&= -\omega \times Z_{term} \\
\log(SPI) &= \log(-\omega) + \log(Z_{term}).
\end{aligned}
\tag{A1}
$$

This decomposition demonstrates that changes in $\log(SPI)$ are driven equally by additive contributions from changes in $\log(-\omega)$ and $\log(Z_{term})$. To assess these contributions over time, we analyze fluctuations in all three terms across the historical and projected record (Fig. A4). We find that $\log(Z_{term})$ exhibits minimal annual and decadal variability. Additionally, interannual and decadal variations in $\log(SPI)$ closely track those in $\log(-\omega)$, indicating that changes in SPI—and consequently in parameterized TC activity—are primarily driven by fluctuations in vertical velocity rather than vorticity. Given this negligible role of vorticity, we largely disregard its influence on approximated TC activity in this report.

References

Bhatia, K., G. A. Vecchi, H. Murakami, S. Underwood, and J. P. Kossin, 2018: Projected response of tropical cyclone intensity and intensification in a global climate model. *Journal of Climate*, **31 (20)**, 8281–8298, https://doi.org/10.1175/JCLI-D-17-0898.1.

Booth, B. B. B., N. J. Dunstone, P. R. Halloran, T. Andrews, and N. Bellouin, 2012: Aerosols implicated as a prime driver of twentieth-century north atlantic climate variability. *Nature*, **484 (7393)**, 228–232, https://doi.org/10.1038/nature10946.

Bretherton, C. S., J. R. McCaa, and H. Grenier, 2004: A new parameterization for shallow cumulus convection and its application to marine subtropical cloud-topped boundary layers. part i: Description and 1d results. *Monthly Weather Review*, **132 (4)**, 864–882, https://doi.org/10.1175/1520-0493(2004)132⟨0864:ANPFSC⟩2.0.CO;2.

Broccoli, A. J., and S. Manabe, 1990: Can existing climate models be used to study anthropogenic changes in tropical cyclone climate? *Geophysical Research Letters*, **17 (11)**, 1917–1920, https://doi.org/10.1029/GL017i011p01917.

Bruyère, C. L., G. J. Holland, and E. Towler, 2012: Investigating the use of a genesis potential index for tropical cyclones in the north atlantic basin. *Journal of Climate*, **25 (24)**, 8611–8626, https://doi.org/10.1175/JCLI-D-11-00619.1.

Camargo, S. J., M. K. Tippett, A. H. Sobel, G. A. Vecchi, and M. Zhao, 2014: Testing the performance of tropical cyclone genesis indices in future climates using the hiram model. *Journal of Climate*, **27 (24)**, 9171–9196, https://doi.org/10.1175/JCLI-D-13-00505.1.

Camargo, S. J., and Coauthors, 2020: Characteristics of model tropical cyclone climatology and the large-scale environment. *Journal of Climate*, **33 (11)**, 4463–4483, https://doi.org/10.1175/JCLI-D-19-0500.1.

Cavicchia, L., E. Scoccimarro, G. Ascenso, A. Castelletti, M. Giuliani, and S. Gualdi, 2023: Tropical cyclone genesis potential indices in a new high-resolution climate models ensemble: Limitations and way forward. *Geophysical Research Letters*, **50 (11)**, e2023GL103 001, https://doi.org/10.1029/2023GL103001.

Chan, D., G. A. Vecchi, W. Yang, and P. Huybers, 2021: Improved simulation of 19th- and 20th-century north atlantic hurricane frequency after correcting historical sea surface temperatures. *Science Advances*, **7 (26)**, eabg6931, https://doi.org/10.1126/sciadv.abg6931.

Chen, J.-H., and S.-J. Lin, 2011: The remarkable predictability of interannual variability of atlantic hurricanes during the past decade. *Geophysical Research Letters*, **38 (11)**, L11 804, https://doi.org/10.1029/2011GL047629.

Cheng, W., J. C. H. Chiang, and D. Zhang, 2013: Atlantic meridional overturning circulation (AMOC) in CMIP5 models: Rcp and historical simulations. *Journal of Climate*, **26 (18)**, 7187–7198, https://doi.org/10.1175/JCLI-D-12-00496.1.

Colbert, A. J., and B. J. Soden, 2012: Climatological variations in north atlantic tropical cyclone tracks. *Journal of Climate*, **25 (2)**, 657–673, https://doi.org/10.1175/JCLI-D-11-00034.1.

Diamond, M. S., 2023: Detection of large-scale cloud microphysical changes within a major shipping corridor after implementation of the international maritime organization 2020 fuel sulfur regulations. *Atmospheric Chemistry and Physics*, **23 (14)**, 8259–8269, https://doi.org/10.5194/acp-23-8259-2023.

Dunstone, N. J., D. M. Smith, B. B. B. Booth, L. Hermanson, and R. Eade, 2013: Anthropogenic aerosol forcing of atlantic tropical storms. *Nature Geoscience*, **6 (7)**, 534–539, https://doi.org/10.1038/ngeo1854.

Emanuel, K., 2010: Tropical cyclone activity downscaled from noaa–cires reanalysis, 1908–1958. *Journal of Advances in Modeling Earth Systems*, **2 (1)**, 1–12, https://doi.org/10.3894/JAMES.2010.2.1.

Emanuel, K., 2021a: Atlantic tropical cyclones downscaled from climate reanalyses show increasing activity over past 150 years. *Nature Communications*, **12 (1)**, 7027, https://doi.org/10.1038/s41467-021-27364-8.

Emanuel, K., 2021b: Response of global tropical cyclone activity to increasing co_2: Results from downscaling cmip6 models. *Journal of Climate*, **34 (1)**, 57–70, https://doi.org/10.1175/JCLI-D-20-0367.1.

Emanuel, K., 2022: Tropical cyclone seeds, transition probabilities, and genesis. *Journal of Climate*, **35 (11)**, 3629–3643, https://doi.org/10.1175/JCLI-D-21-0922.1.

Emanuel, K., and D. Nolan, 2004: Tropical cyclone activity and global change. *Proceedings, 26th Conference on Hurricanes and Tropical Meteorology*, Miami, FL, American Meteorological Society, P2.2, URL https://ams.confex.com/ams/26HURR/techprogram/paper_75463.htm.

Emanuel, K., S. Solomon, D. Folini, S. Davis, and C. Cagnazzo, 2013: Influence of tropical tropopause layer cooling on atlantic hurricane activity. *Journal of Climate*, **26 (7)**, 2288–2303, https://doi.org/10.1175/JCLI-D-12-00242.1.

Emanuel, K., R. Sundararajan, and J. Williams, 2008: Hurricanes and global warming: Results from downscaling IPCC AR4 simulations. *Bulletin of the American Meteorological Society*, **89 (3)**, 347–367, https://doi.org/10.1175/BAMS-89-3-347.

Emanuel, K. A., 2013: Downscaling CMIP5 climate models shows increased tropical cyclone activity over the 21st century. *Proceedings of the National Academy of Sciences*, **110 (30)**, 12 219–12 224, https://doi.org/10.1073/pnas.1301293110.

Eusebi, R., W. Yang, G. A. Vecchi, and S. Fueglistaler, 2025: Statistical modeling of north atlantic hurricane frequency and the impact and role of patterned warming. *Journal of Climate*, **38 (19)**, 5391–5410, https://doi.org/10.1175/JCLI-D-24-0647.1.

Flannaghan, T. J., S. Fueglistaler, I. M. Held, S. Po-Chedley, B. Wyman, and M. Zhao, 2014: Tropical temperature trends in atmospheric general circulation model simulations and the impact of uncertainties in observed SSTs. *Journal of Geophysical Research: Atmospheres*, **119 (23)**, 13 327–13 337, https://doi.org/10.1002/2014JD022365.

Fueglistaler, S., C. Radley, and I. M. Held, 2015: The distribution of precipitation and the spread in tropical upper tropospheric temperature trends in CMIP5/AMIP simulations. *Geophysical Research Letters*, **42 (14)**, 6000–6007, https://doi.org/10.1002/2015GL064966.

Gelaro, R., and Coauthors, 2017: The modern-era retrospective analysis for research and applications, version 2 (MERRA-2). *Journal of Climate*, **30 (14)**, 5419–5454, https://doi.org/10.1175/JCLI-D-16-0758.1.

Goldenberg, S. B., C. W. Landsea, A. M. Mestas-Nuñez, and W. M. Gray, 2001: The recent increase in atlantic hurricane activity: Causes and implications. *Science*, **293 (5529)**, 474–479, https://doi.org/10.1126/science.1060040.

Harris, L. M., S.-J. Lin, and C. Tu, 2016: High-resolution climate simulations using GFDL HiRAM with a stretched global grid. *Journal of Climate*, **29 (11)**, 4293–4314, https://doi.org/10.1175/JCLI-D-15-0389.1.

Held, I. M., and B. J. Soden, 2000: Water vapor feedback and global warming. *Annual Review of Environment and Resources*, **25**, 441–475, https://doi.org/10.1146/annurev.energy.25.1.441.

Hersbach, H., and Coauthors, 2020: The ERA5 global reanalysis. *Quarterly Journal of the Royal Meteorological Society*, **146 (730)**, 1999–2049, https://doi.org/10.1002/qj.3803.

Hsieh, T.-L., G. A. Vecchi, W. Yang, I. M. Held, and S. T. Garner, 2020: Large-scale control on the frequency of tropical cyclones and seeds: a consistent relationship across a hierarchy of global atmospheric models. *Climate Dynamics*, **55 (11)**, 3177–3196, https://doi.org/10.1007/s00382-020-05446-5.

Hsieh, T.-L., W. Yang, G. A. Vecchi, and M. Zhao, 2022: Model spread in the tropical cyclone frequency and seed propensity index across global warming and enso-like perturbations. *Geophysical Research Letters*, **49 (7)**, e2021GL097 157, https://doi.org/10.1029/2021GL097157.

Hsieh, T.-L., B. Zhang, W. Yang, G. A. Vecchi, M. Zhao, B. J. Soden, and C. Wang, 2023: The influence of large-scale radiation anomalies on tropical cyclone frequency. *Journal of Climate*, **36 (16)**, 5431–5441, https://doi.org/10.1175/JCLI-D-22-0449.1.

Ikehata, K., and M. Satoh, 2021: Climatology of tropical cyclone seed frequency and survival rate in tropical cyclones. *Geophysical Research Letters*, **48 (18)**, e2021GL093 626, https://doi.org/10.1029/2021GL093626.

Jordan, G., and M. Henry, 2024: IMO2020 regulations accelerate global warming by up to 3 years in UKESM1. *Earth's Future*, **12 (8)**, e2024EF005 011, https://doi.org/10.1029/2024EF005011.

Klotzbach, P. J., 2011a: El niño–southern oscillation's impact on atlantic basin hurricanes and u.s. landfalls. *Journal of Climate*, **24 (4)**, 1252–1263, https://doi.org/10.1175/2010JCLI3799.1.

Klotzbach, P. J., 2011b: The influence of el niño–southern oscillation and the atlantic multidecadal oscillation on caribbean tropical cyclone activity. *Journal of Climate*, **24 (3)**, 721–731, https://doi.org/10.1175/2010JCLI3705.1.

Klotzbach, P. J., S. G. Bowen, R. Pielke, and M. Bell, 2018: Continental u.s. hurricane landfall frequency and associated damage: Observations and future risks. *Bulletin of the American Meteorological Society*, **99 (7)**, 1359–1376, https://doi.org/10.1175/BAMS-D-17-0184.1.

Klotzbach, P. J., K. M. Wood, C. J. Schreck III, S. G. Bowen, C. M. Patricola, and M. M. Bell, 2022: Trends in global tropical cyclone activity: 1990–2021. *Geophysical Research Letters*, **49 (6)**, e2021GL095 774, https://doi.org/10.1029/2021GL095774.

Knutson, T., and Coauthors, 2020: Tropical cyclones and climate change assessment: Part II: Projected response to anthropogenic warming. *Bulletin of the American Meteorological Society*, **101 (3)**, E303–E322, https://doi.org/10.1175/BAMS-D-18-0194.1.

Knutson, T. R., J. J. Sirutis, Ming Zhao, R. E. Tuleya, M. Bender, G. A. Vecchi, G. Villarini, and D. Chavas, 2015: Global projections of intense tropical cyclone activity for the late twenty-first century from dynamical downscaling of CMIP5/RCP4.5 scenarios. **28 (18)**, 7203–7224, https://doi.org/10.1175/JCLI-D-15-0129.1.

Kortum, G., G. A. Vecchi, T.-L. Hsieh, and W. Yang, 2024: Influence of weather and climate on multidecadal trends in atlantic hurricane genesis and tracks. *Journal of Climate*, **37 (5)**, 1501–1522, https://doi.org/10.1175/JCLI-D-23-0088.1.

Kossin, J. P., and S. J. Camargo, 2009: Hurricane track variability and secular potential intensity trends. *Climatic Change*, **97 (1)**, 329–337, https://doi.org/10.1007/s10584-009-9748-2.

Kossin, J. P., K. R. Knapp, T. L. Olander, and C. S. Velden, 2020: Global increase in major tropical cyclone exceedance probability over the past four decades. **117 (22)**, 11 975–11 980, https://doi.org/10.1073/pnas.1920849117.

Laloyaux, P., and Coauthors, 2018: CERA-20C: a coupled reanalysis of the twentieth century. *J. Adv. Model. Earth Syst.*, **10**, 1172–1195, https://doi.org/10.1029/2018MS001273.

Lee, C.-Y., S. J. Camargo, A. H. Sobel, and M. K. Tippett, 2020: Statistical–dynamical downscaling projections of tropical cyclone activity in a warming climate: Two diverging genesis scenarios. *Journal of Climate*, **33 (11)**, 4201–4221, https://doi.org/10.1175/JCLI-D-19-0452.1.

Lee, C.-Y., A. H. Sobel, M. K. Tippett, S. J. Camargo, M. Wüest, M. Wehner, and H. Murakami, 2023: Climate change signal in atlantic tropical cyclones today and near future. *Earth's Future*, **11 (11)**, e2023EF003 539, https://doi.org/10.1029/2023EF003539.

Manganello, J. V., and Coauthors, 2012: Tropical cyclone climatology in a 10-km global atmospheric gcm: Toward weather-resolving climate modeling. *Journal of Climate*, **25 (11)**, 3867–3893, https://doi.org/10.1175/JCLI-D-11-00346.1.

Mann, M. E., and K. A. Emanuel, 2006: Atlantic hurricane trends linked to climate change. *Eos, Transactions American Geophysical Union*, **87 (24)**, 233–241, https://doi.org/10.1029/2006EO240001.

Murakami, H., and B. Wang, 2022: Patterns and frequency of projected future tropical cyclone genesis are governed by dynamic effects. *Communications Earth & Environment*, **3 (1)**, 1–10, https://doi.org/10.1038/s43247-022-00410-z.

Neelin, J. D., and I. M. Held, 1987: Modeling tropical convergence based on the moist static energy budget. *Monthly Weather Review*, **115 (1)**, 3–12, https://doi.org/10.1175/1520-0493(1987)115⟨0003:MTCBOT⟩2.0.CO;2.

Olszewski, K., 1986: Saturation deficit in various air masses. *Miscellanea Geographica*, **2 (1)**, 79–84, https://doi.org/10.2478/mgrsd-1986-020111.

Patricola, C. M., P. Chang, and R. Saravanan, 2016: Degree of simulated suppression of atlantic tropical cyclones modulated by flavour of el niño. *Nature Geoscience*, **9 (2)**, 155–160, https://doi.org/10.1038/ngeo2624.

Patricola, C. M., R. Saravanan, and P. Chang, 2018: The response of atlantic tropical cyclones to suppression of african easterly waves. *Geophysical Research Letters*, **45 (1)**, 471–479, https://doi.org/10.1002/2017GL076081.

Pfahl, S., P. A. O'Gorman, and E. M. Fischer, 2017: Understanding the regional pattern of projected future changes in extreme precipitation. *Nature Climate Change*, **7 (6)**, 423–427, https://doi.org/10.1038/nclimate3287.

Pielke, R. A., and C. N. Landsea, 1999: La niña, el niño, and atlantic hurricane damages in the united states. *Bulletin of the American Meteorological Society*, **80 (10)**, 2027–2033.

Ramsay, H. A., and A. H. Sobel, 2011: Effects of relative and absolute sea surface temperature on tropical cyclone potential intensity using a single-column model. *Journal of Climate*, **24 (1)**, 183–193, https://doi.org/10.1175/2010JCLI3690.1.

Ritchie, E. A., and G. J. Holland, 1999: Large-scale patterns associated with tropical cyclogenesis in the western pacific. *Monthly Weather Review*, **127 (9)**, 2027–2043, https://doi.org/10.1175/1520-0493(1999)127⟨2027:LSPAWT⟩2.0.CO;2.

Seager, R., N. Henderson, and M. Cane, 2022: Persistent discrepancies between observed and modeled trends in the tropical pacific ocean. *Journal of Climate*, **35 (14)**, 4571–4584, https://doi.org/10.1175/JCLID210648.1.

Shaw, T. A., and Coauthors, 2024: Regional climate change: consensus, discrepancies, and ways forward. *Frontiers in Climate*, **6**, 1–14, https://doi.org/10.3389/fclim.2024.1391634.

Sobel, A. H., I. M. Held, and C. S. Bretherton, 2002: The enso signal in tropical tropospheric temperature. *Journal of Climate*, **15 (18)**, 2702–2708, https://doi.org/10.1175/1520-0442(2002)015⟨2702:TESITT⟩2.0.CO;2.

Sobel, A. H., A. A. Wing, S. J. Camargo, C. M. Patricola, G. A. Vecchi, C. Lee, and M. K. Tippett, 2021: Tropical cyclone frequency. *Earth's Future*, **9 (12)**, e2021EF002 275, https://doi.org/10.1029/2021EF002275.

Srokosz, M., and H. Bryden, 2015: Observing the atlantic meridional overturning circulation yields a decade of inevitable surprises. *Science*, **348 (6241)**, 1255 575, https://doi.org/10.1126/science.1255575.

Sugi, M., Y. Yamada, K. Yoshida, R. Mizuta, M. Nakano, C. Kodama, and M. Satoh, 2020: Future changes in the global frequency of tropical cyclone seeds. *SOLA*, **16**, 70-74, https://doi.org/10.2151/sola.2020012.

Tang, B., and S. J. Camargo, 2014: Environmental control of tropical cyclones in cmip5: A ventilation perspective. *Journal of Advances in Modeling Earth Systems*, **6 (1)**, 115-128, https://doi.org/10.1002/2013MS000294.

Tang, B., and K. Emanuel, 2010: Midlevel ventilation's constraint on tropical cyclone intensity. *Journal of the Atmospheric Sciences*, **67 (6)**, 1817-1830, https://doi.org/10.1175/2010JAS3318.1.

Tang, B., and K. Emanuel, 2012: A ventilation index for tropical cyclones. *Bulletin of the American Meteorological Society*, **93 (12)**, 1901-1915, https://doi.org/10.1175/BAMSD1100165.1.

Taylor, K. E., R. J. Stouffer, and G. A. Meehl, 2012: An overview of CMIP5 and the experiment design. https://doi.org/10.1175/BAMS-D-11-00094.1.

Tippett, M., S. Camargo, and A. Sobel, 2011: A poisson regression index for tropical cyclone genesis and the role of large-scale vorticity in genesis. *Journal of Climate*, **24 (9)**, 2335-2357, https://doi.org/10.1175/2010JCLI3811.1.

Vecchi, G. A., S. Fueglistaler, I. M. Held, T. R. Knutson, and M. Zhao, 2013: Impacts of atmospheric temperature trends on tropical cyclone activity. *Journal of Climate*, **26 (11)**, 3877–3898, https://doi.org/10.1175/JCLI-D-12-00503.1.

Vecchi, G. A., and T. R. Knutson, 2008: On estimates of historical north atlantic tropical cyclone activity. *Journal of Climate*, **21 (14)**, 3580–3600, https://doi.org/10.1175/2008JCLI2178.1.

Vecchi, G. A., and T. R. Knutson, 2011: Estimating annual numbers of atlantic hurricanes missing from the hurdat database (1878–1965) using ship track density. *Journal of Climate*, **24 (6)**, 1736–1746, https://doi.org/10.1175/2010JCLI3810.1.

Vecchi, G. A., C. Landsea, W. Zhang, G. Villarini, and T. Knutson, 2021: Changes in atlantic major hurricane frequency since the late-19th century. *Nature Communications*, **12 (1)**, 4054, https://doi.org/10.1038/s41467-021-24268-5.

Vecchi, G. A., and B. J. Soden, 2007: Effect of remote sea surface temperature change on tropical cyclone potential intensity. *Nature*, **450 (7172)**, 1066–1070, https://doi.org/10.1038/nature06423.

Vecchi, G. A., M. Zhao, H. Wang, G. Villarini, A. Rosati, A. Kumar, I. M. Held, and R. Gudgel, 2011: Statistical–dynamical predictions of seasonal north atlantic hurricane activity. *Monthly Weather Review*, **139 (4)**, 1070–1082, https://doi.org/10.1175/2010MWR3499.1.

Vecchi, G. A., and Coauthors, 2019: Tropical cyclone sensitivities to co2 doubling: roles of atmospheric resolution, synoptic variability and background climate changes. *Climate Dynamics*, **53 (9)**, 5999–6033, https://doi.org/10.1007/s00382-019-04913-y.

Villarini, G., G. A. Vecchi, T. R. Knutson, and J. A. Smith, 2011a: Is the recorded increase in short-duration north atlantic tropical storms spurious? *Journal of Geophysical Research: Atmospheres*, **116**, D10 112, https://doi.org/10.1029/2010JD015493.

Villarini, G., G. A. Vecchi, T. R. Knutson, M. Zhao, and J. A. Smith, 2011b: North atlantic tropical storm frequency response to anthropogenic forcing: Projections and sources of uncertainty. *Journal of Climate*, **24 (13)**, 3224–3248, https://doi.org/10.1175/2011JCLI3853.1.

Villarini, G., G. A. Vecchi, and J. A. Smith, 2010: Modeling the dependence of tropical storm counts in the north atlantic basin on climate indices. *Monthly Weather Review*, **138 (7)**, 2681–2705, https://doi.org/10.1175/2010MWR3315.1.

Walsh, K. J. E., S. J. Camargo, T. R. Knutson, J. Kossin, T.-C. Lee, H. Murakami, and C. Patricola, 2019: Tropical cyclones and climate change. *Tropical Cyclone Research and Review*, **8 (4)**, 240–250, https://doi.org/10.1016/j.tcrr.2020.01.004.

Wang, B., and H. Murakami, 2020: Dynamic genesis potential index for diagnosing present-day and future global tropical cyclone genesis. *Environmental Research Letters*, **15 (11)**, 114 008, https://doi.org/10.1088/1748-9326/abbb01.

Weller, E., S.-K. Min, W. Cai, F. W. Zwiers, Y.-H. Kim, and D. Lee, 2016: Human-caused indo-pacific warm pool expansion. *Science Advances*, **2 (7)**, e1501 719, https://doi.org/10.1126/sciadv.1501719.

Xie, L., T. Yan, L. J. Pietrafesa, J. M. Morrison, and T. Karl, 2005: Climatology and interannual variability of north atlantic hurricane tracks. *Journal of Climate*, **18 (24)**, 5370–5381, https://doi.org/10.1175/JCLI3560.1.

Yamada, Y., and Coauthors, 2021: Evaluation of the contribution of tropical cyclone seeds to changes in tropical cyclone frequency due to global warming in high-resolution multi-model ensemble simulations. *Progress in Earth and Planetary Science*, **8 (1)**, 11, https://doi.org/10.1186/s40645-020-00397-1.

Yang, W., T.-L. Hsieh, and G. A. Vecchi, 2021: Hurricane annual cycle controlled by both seeds and genesis probability. *Proceedings of the National Academy of Sciences*, **118 (41)**, e2108397 118, https://doi.org/10.1073/pnas.2108397118.

Zhang, B., B. J. Soden, G. A. Vecchi, and W. Yang, 2021: The role of radiative interactions in tropical cyclone development under realistic boundary conditions. *Journal of Climate*, **34 (6)**, 2079–2091, https://doi.org/10.1175/JCLI-D-20-0574.1.

Zhang, C., 1993: Large-scale variability of atmospheric deep convection in relation to sea surface temperature in the tropics. *Journal of Climate*, **6 (10)**, 1898–1913, https://doi.org/10.1175/1520-0442(1993)006⟨1898:LSVOAD⟩2.0.CO;2.

Zhang, J., Y.-S. Chen, E. Gryspeerdt, T. Yamaguchi, and G. Feingold, 2025: Radiative forcing from the 2020 shipping fuel regulation is large but hard to detect. *Communications Earth & Environment*, **6 (1)**, 1–11, https://doi.org/10.1038/s43247-024-01911-9.

Zhang, R., and T. L. Delworth, 2006: Impact of atlantic multidecadal oscillations on india/sahel rainfall and atlantic hurricanes. *Geophysical Research Letters*, **33 (17)**, L17 712, https://doi.org/10.1029/2006GL026267.

Zhao, M., and I. M. Held, 2010: An analysis of the effect of global warming on the intensity of atlantic hurricanes using a gcm with statistical refinement. *Journal of Climate*, **23 (23)**, 6382–6395, https://doi.org/10.1175/2010JCLI3837.1.

Zhao, M., I. M. Held, S.-J. Lin, and G. A. Vecchi, 2009: Simulations of global hurricane climatology, interannual variability, and response to global warming using a 50-km resolution gcm. *Journal of Climate*, **22 (24)**, 6653–6678, https://doi.org/10.1175/2009JCLI3049.1.

Zhuo, J.-Y., C.-Y. Lee, A. Sobel, R. Seager, S. J. Camargo, Y.-H. Lin, B. Fosu, and K. A. Reed, 2025: A more La Niña–like response to radiative forcing after flux adjustment in CESM2. *Journal of Climate*, **38 (4)**, 1321–1346, https://doi.org/10.1175/JCLI-D-24-0331.1.